



## RESEARCH ARTICLE

10.1002/2015GC006095

## Rock magnetic expression of fluid infiltration in the Yingxiu-Beichuan fault (Longmen Shan thrust belt, China)

Tao Yang<sup>1,2</sup>, Xiaosong Yang<sup>3</sup>, Qingbao Duan<sup>3</sup>, Jianye Chen<sup>3,4</sup>, and Mark J. Dekkers<sup>2</sup>

## Key Points:

- Links of magnetic, mineral, and chemical properties of fault rocks are shown
- Magnetite depletion in fault rocks indicates involvement of fluid infiltration
- Fluid-rock interaction in fault zones can be traced by magnetic properties

## Correspondence to:

T. Yang,  
yangtao@cea-igp.ac.cn

## Citation:

Yang, T., X. Yang, Q. Duan, J. Chen, and M. J. Dekkers (2016), Rock magnetic expression of fluid infiltration in the Yingxiu-Beichuan fault (Longmen Shan thrust belt, China), *Geochem. Geophys. Geosyst.*, 17, 1065–1085, doi:10.1002/2015GC006095.

Received 10 SEP 2015

Accepted 25 FEB 2016

Accepted article online 1 MAR 2016

Published online 22 MAR 2016

<sup>1</sup>Key Laboratory of Seismic Observation and Geophysical Imaging, Institute of Geophysics, China Earthquake Administration, Beijing, China, <sup>2</sup>Paleomagnetic Laboratory Fort Hoofddijk, Department of Earth Sciences, Utrecht University, Utrecht, Netherlands, <sup>3</sup>State Key Laboratory of Earthquake Dynamics, Institute of Geology, China Earthquake Administration, Beijing, China, <sup>4</sup>HPT Laboratory, Department of Earth Sciences, Utrecht University, Utrecht, Netherlands

**Abstract** Fluid infiltration within fault zones is an important process in earthquake rupture. Magnetic properties of fault rocks convey essential clues pertaining to physicochemical processes in fault zones. In 2011, two shallow holes (134 and 54 m depth, respectively) were drilled into the Yingxiu-Beichuan fault (Longmen Shan thrust belt, China), which accommodated most of the displacement of the 2008 Mw 7.9 Wenchuan earthquake. Fifty-eight drill core samples, including granitic host rock and various fault rocks, were analyzed rock-magnetically, mineralogically, and geochemically. The magnetic behavior of fault rocks appears to be dominated by paramagnetic clay minerals. Magnetite in trace amounts is identified as the predominant ferrimagnetic fraction in all samples, decreasing from the host rock, via fault breccia to (proto-)cataclasite. Significant mass-losses (10.7–45.6%) are determined for the latter two with the “isocon” method. Volatile contents and alteration products (i.e., chlorite) are enriched toward the fault core relative to the host rocks. These observations suggest that magnetite depletion occurred in these fault rocks—exhumed from the shallow crust—plumbed by fluid-assisted processes. Chlorite, interpreted to result from hydrothermal activity, occurs throughout almost the entire fault core and shows high coefficients of determination ( $R^2 > 0.6$ ) with both low and high-field magnetic susceptibility. Close relationships, with  $R^2 > 0.70$ , are also observed between both low and high-field magnetic susceptibility and the immobile elements (e.g.,  $\text{TiO}_2$ ,  $\text{P}_2\text{O}_5$ ,  $\text{MnO}$ ),  $\text{H}_2\text{O}^+$ , and the calculated mass-losses of fault rocks. Hence, magnetic properties of fault rocks can serve as proxy indicators of fluid infiltration within shallow fault zones.

## 1. Introduction

Fluid infiltration within fault zones plays a critical role in physical, chemical, and mechanical evolution of fault rocks [Goddard and Evans, 1995; Chen et al., 2007; Isaacs et al., 2007; Ishikawa et al., 2008; Niwa et al., 2015]. In particular, the presence of fault fluid is intimately linked to the nucleation, propagation, arrest, and recurrence of earthquake ruptures [Hickman et al., 1995; Zoback et al., 2007]. Thus, the study of fault rocks that record rock-fluid interaction processes is important for understanding the deformation mechanism(s) and evolution history of faults. The behavior of fluid in fault zones has been investigated by examining mineral assemblages, chemical compositions, and structural textures of fault rocks in well-exposed fault zones [e.g., Goddard and Evans, 1995; Tanaka et al., 2001; Chen et al., 2013]. Furthermore, several faults where recent earthquakes occurred were drilled and cored to examine the fault rocks and their relation to seismic rupturing. Examples include the Nojima Fault Probe Project after the 1995 Mw 6.9 Kobe earthquake [e.g., Tanaka et al., 2001], the Taiwan Chelungpu fault Drilling Project (TCDP) after the 1999 Mw 7.6 Chi-Chi earthquake [e.g., Chen et al., 2007; Ishikawa et al., 2008; Kuo et al., 2009], and the recent Wenchuan earthquake Fault Scientific Drilling (WFSD-1) project after the 2008 Mw 7.9 Wenchuan earthquake [e.g., Li et al., 2014; Si et al., 2014].

Fluids in fault zones derive from multiple sources, including deeply circulating meteoric waters that can penetrate the upper ~10 to ~15 km of the crust [Kerrick and Kammerini, 1988], trapped formation brines, fluids from mineral dehydration during prograde metamorphism, and release of volatiles from molten magma or the upper mantle [Hickman et al., 1995; Zoback et al., 2007]. In general, fault zones are a dense network of fractures and secondary faults; fault rocks can be susceptible to disaggregation and dissolution by fluids during co, post, and interseismic periods. Destabilization of iron-bearing (clay) minerals in fault zones will

release ferrous Fe that easily enters the fluid and is subsequently transported [Grosz *et al.*, 2006; Hashimoto and Kaji, 2012; Just and Kontny, 2012]. The Fe-rich fluids are potential sources to precipitate magnetic minerals [Pechersky and Genshaft, 2001]. Furthermore, migration paths and compositions of these fluids vary markedly over time and space, as fault zones act as fluid-flow conduits or barriers at different stages in their development [Goddard and Evans, 1995]. This leads to temporal and spatial changes in redox state of a fault zone as function of episodic fault rupture and recovery cycles during the lifetime of the fault [Yamaguchi *et al.*, 2011]. Thus fluid circulation may precipitate fine-grained iron-oxides (e.g., magnetite), hydroxides (e.g., goethite and lepidocrocite), and/or sulfides (e.g., pyrite) under different physicochemical conditions (temperature, redox, pH, fluid-rock ratio, etc.) [Goldstein and Brown, 1988; Grosz *et al.*, 2006; Guichet *et al.*, 2006]. Thus, these Fe-bearing (which includes the magnetic) minerals reveal information on rock-fluid interactions within fault zones. Due to their trace concentration and/or imperfect crystallinity, however, the magnetic minerals are usually difficult to be identified—i.e., below the detection limit of the technique employed—by the more conventionally applied mineralogical and geochemical methods, such as electron spin resonance or X-ray diffraction (XRD) [Fukuchi, 2003]. On the other hand, magnetic measurements can readily offer information on mineralogy, concentration, and granulometry of magnetic minerals. Examining mineral magnetic properties of fault rocks thus can be expected to yield valuable insights into characteristics of fluid in relation to evolution and features of fault zones, where alteration/neoformation of magnetic minerals as a result of fluid introduction occurs during co, post and interseismic periods [Chou *et al.*, 2012a, 2012b; Yang *et al.*, 2013].

Up to now, most rock magnetic studies on fault rocks were focused on unraveling magnetic changes associated with thermal decomposition due to seismic frictional heating [e.g., Hirono *et al.*, 2006; Mishima *et al.*, 2006; Tanikawa *et al.*, 2008; Yang *et al.*, 2012a, 2012b; Liu *et al.*, 2014; Pei *et al.*, 2014a, 2014b], the magnetic record of coseismic electrical currents [e.g., Enomoto and Zheng, 1998; Ferré *et al.*, 2005], and magnetization acquisition mechanisms [e.g., Ferré *et al.*, 2012]. However, only a few of those studies have examined rock-fluid interactions in fault zones. For example, a marked contrast between magnetic properties of two components of fault breccias (fragments and matrix) has been reported by Yang *et al.* [2013] in the 2008 Wenchuan earthquake rupture zone. The main reason for this variation is considered to be fault fluids that induced selective dissolution and precipitation of Fe-bearing minerals. Furthermore, in the 16 cm thick gouge within the Taiwan Chelungpu fault, which hosted the principal slip zone of the 1999 Mw 7.6 Chi-Chi earthquake, the collective observation of retrograde alteration of pyrrhotite and partially oxidized magnetite suggests hot aqueous coseismic fluid (>350°C) was percolating within the fault zone during the 1999 Chi-Chi event [Chou *et al.*, 2012a]. During cooling of these fluids, goethite was formed within the gouge. Hence, it is believed that fluid infiltration has profound influence on magnetic mineralogy of fault rocks during both the instantaneous co-seismic and the long-term interseismic periods. Turning the argument around, magnetic properties of fault rocks convey important clues pertaining to physical and chemical processes in a fault zone.

The present study involves fault rocks from the active Yingxiu-Beichuan fault (YBF) in the Longmen Shan (LMS) thrust belt (Figure 1). The 2008 Wenchuan earthquake produced a north-northeast-striking rupture over a length of ~270 km along the YBF, with maximum displacements amounting to 8.0–10.0 m and 5.0–6.0 m in the vertical and horizontal directions, respectively [Liu-Zeng *et al.*, 2009]. In order to better understand compositional, physical, and chemical characteristics of the fault zone, two shallow holes (LMFD-3A and 3B) were drilled at the Jinhe (also called Golden River) locality (site LMFD-3), at Hongbai Town, Shifang City, Sichuan Province (China) in 2011 (Figures 1 and 2). Microstructural, mineralogical, and geochemical analyses of representative drill core samples suggest that fluids have pervasively infiltrated into the fault zone [Duan *et al.*, 2016]. Here we describe rock magnetic properties of selected samples from the two drill holes, and examine their relationship with mineralogical and chemical compositions, in an effort to explore the potential magnetic record of fluid infiltration.

## 2. Geological Setting and Samples

The LMS thrust belt, approximately 500 km long and 30–50 km wide, is the tectonic boundary between the Tibetan Plateau and the Sichuan Basin. It lies between the Songpan-Ganzi terrane (a Triassic orogenic belt) to the west and the Sichuan Mesozoic-Cenozoic foreland basin on the Yangtze block to the east (Figure 1)

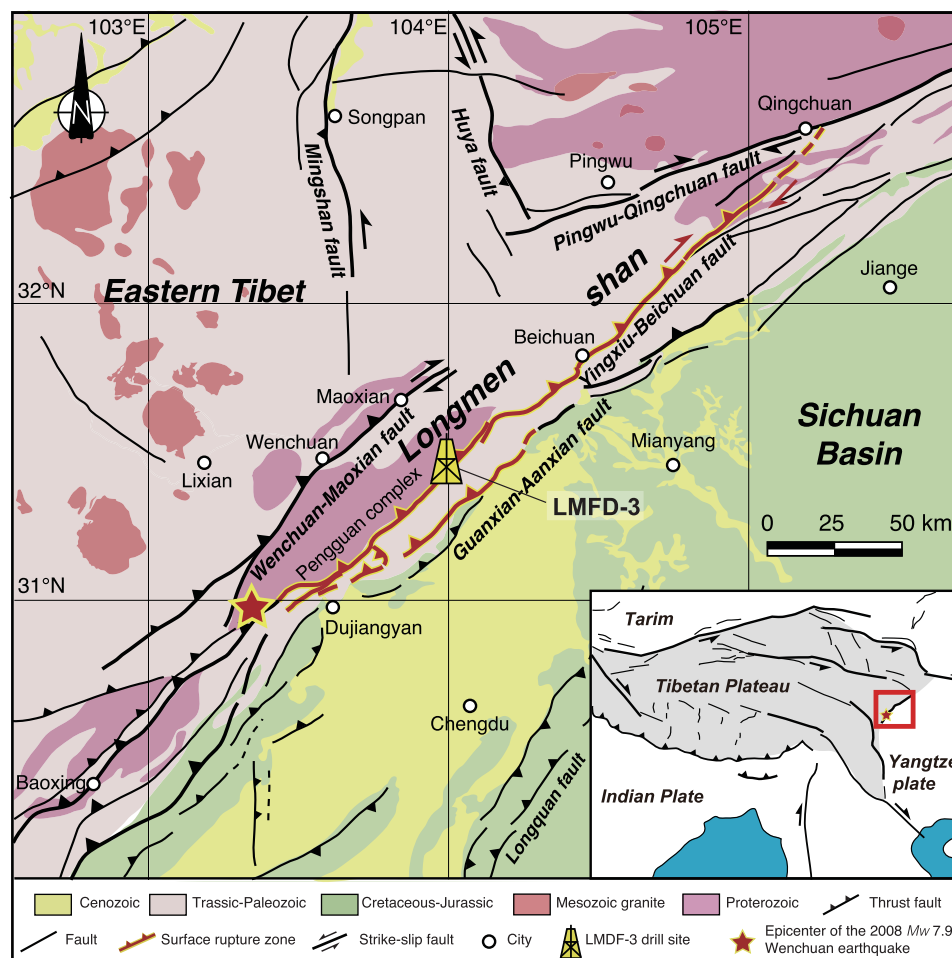


**Figure 1.** Geological map of the central part of the Longmen Shan (LMS) thrust belt (adapted from Wang *et al.* [2015]). The portions of the various fault traces in red-bold mark the coseismic surface ruptures induced by the 2008 Mw 7.9 Wenchuan earthquake (red star). The drill site (LMFD-3) is located in the middle section of the Yingxiu-Beichuan fault (YBF).

[Xu *et al.*, 2008]. The LMS belt is typified by four major northeast-trending thrusts: the aforementioned YBF, and the Wenchuan-Maoxian, Guanxian-Anxian, and Pingwu-Qingchuan faults. As a foreland accretionary wedge, it is lithologically complex, consisting of Precambrian metamorphic rocks (700–800 Ma), with small amounts of Neoproterozoic volcanic rocks and Sinian (Ediacaran) to Early-Middle Triassic marine sedimentary rocks (Figure 1) [Xu *et al.*, 2009].

The Jinhe site (LMFD-3) is located in the central section of the YBF (Figure 1), where the Neoproterozoic Pengguan complex with an age of 850–750 Ma [Yan *et al.*, 2004] overthrusts the Paleozoic carbonates. Here the fault plane strikes N40°E and dips 70–87°NW, and a fault scarp of ~3.4 m vertical displacement (no horizontal displacement was observed at the site) was produced by the 2008 Wenchuan earthquake [Xu *et al.*, 2009]. The structure of the fault zone is rather complicated. From the hanging wall to the footwall, it consists of (1) granite, (2) mafic dyke (diabase), (3) granite, (4) cohesive protocataclite and cataclite, (5) incohesive granitic breccia, (6) fault gouge, and (7) fractured carbonate rock and carbonate host rocks. The fault core of ~4 m width is composed of fault breccia and fault gouge (Figure 2a and 2b).

Two shallow holes were drilled at this site; both of them did not reach the underlying Paleozoic carbonates. The so-called primary hole (hole A) with a total depth of 134 m is located 42 m west of the fault plane (Figure 2b). It penetrated granite (0–14 m), mafic dyke (14–60 m), protocataclite (60–100 m), and cataclite (100–134 m). However, it did not penetrate across the fault core (Figure 2c) because of difficulties during the drilling operation. The secondary hole (hole B) with a total depth of 54 m is located ~15 m west of the fault plane (Figure 2b). It penetrated granite (0–23 m), protocataclite (23–29 m), fractured and weakly

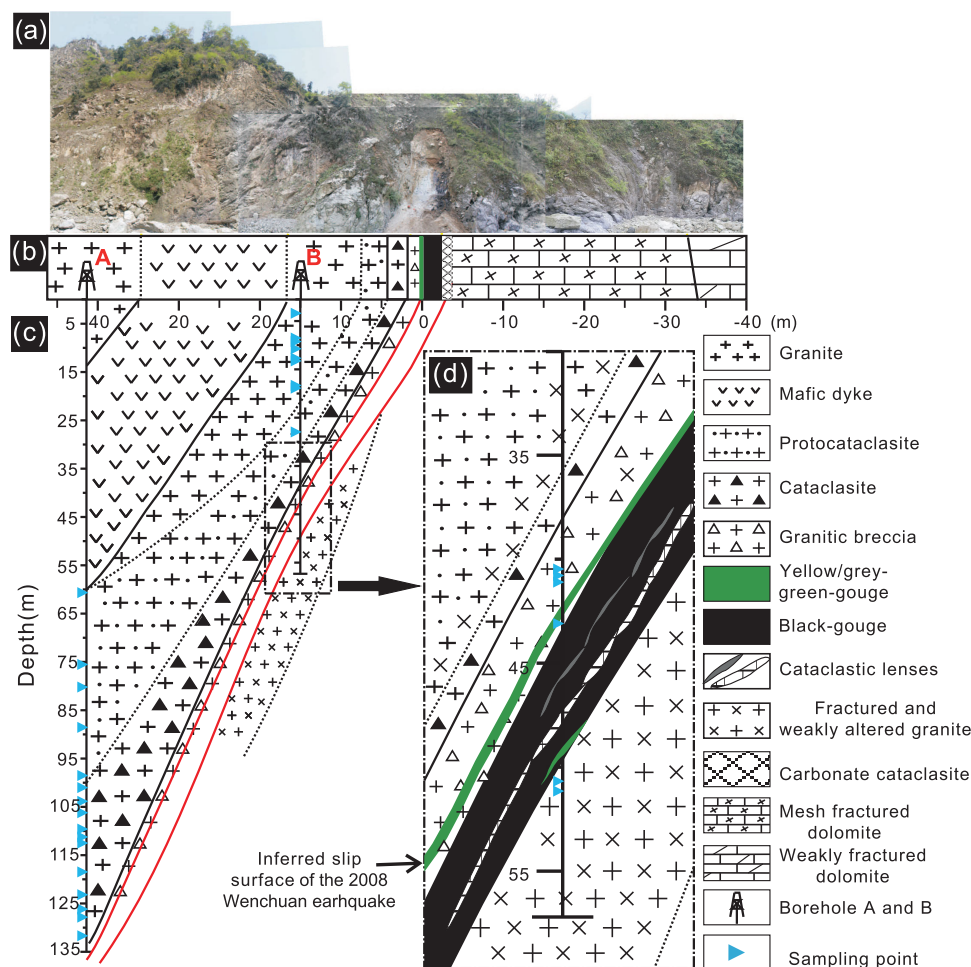


**Figure 2.** (a) Panoramic photograph of the Jinhe exposure of the YBF fault at Hongbai Town, Shifang City, Sichuan Province (China). (b) Sketch of (a) showing the occurrence of the fault zone. Outline and lithological profile of (c) the primary borehole (Hole A) and (d) the secondary hole (Hole B). Triangles mark the sampling points. The reader is referred to Figure 3 for the sampling points in the fault core of Hole B.

altered granite (FWAG; 29–35 and 49.7–54 m), granitic breccia (41.8–41.9 and 42.0–42.5 m), and fault gouge (41.9–49 m) (Figure 2d). So, locally the fault zone cuts through the granitic complex as well. The fault gouge is categorized into three groups according to their colors (Figures 2 and 3). Group I (yellow-green-gouge or YGG) is evidently yellow-green in color; it appears as a thin layer (~10 cm thick between depth of 41.9 and 42.0 m) cutting the granitic breccia, and is inferred to host the principle slip surface of the 2008 Wenchuan earthquake [Duan *et al.*, 2016]. Group II (black-gouge or BG) is black in color and occurs from 42.6 to 47.2 m, while group III (green-grey-gouge or GGG) is grey-green in color and is distributed at depths of 47.3–47.7 and 49.0 m.

Microstructural images of typical fault rocks are shown in Figure 4. The protocataclasite mainly consists of quartz and plagioclase. It has a high density of cracks; typical alteration minerals (e.g., chlorite) can be seen in and along the cracks (Figure 4a). The cataclasite, which predominately consists of quartz and feldspars with minor amounts of biotite and clay minerals, is highly fractured (Figure 4b). Networks of anastomosing micro-shear bands filled with precipitated black and fine-grained material (Figure 4b) can be observed. The granitic breccia consists of fragments (mainly quartz) surrounded by fine-grained matrix (Figure 4c). The depletion in feldspar and enrichment in clays (c.f. Figures 4a–4c) might be indicative of the alteration from one to the other. It is also evident that clasts are remarkably reduced in grain size, perhaps due to pervasive grain comminution and fluid alteration. All the gouge samples show a typical matrix-supported structure, with minor fractured clasts surrounded by fine-grained clay minerals (Figures 4d–4h). Specifically, the BG material is strongly oriented, characterized by black carbonaceous material and calcite veins filling in cracks

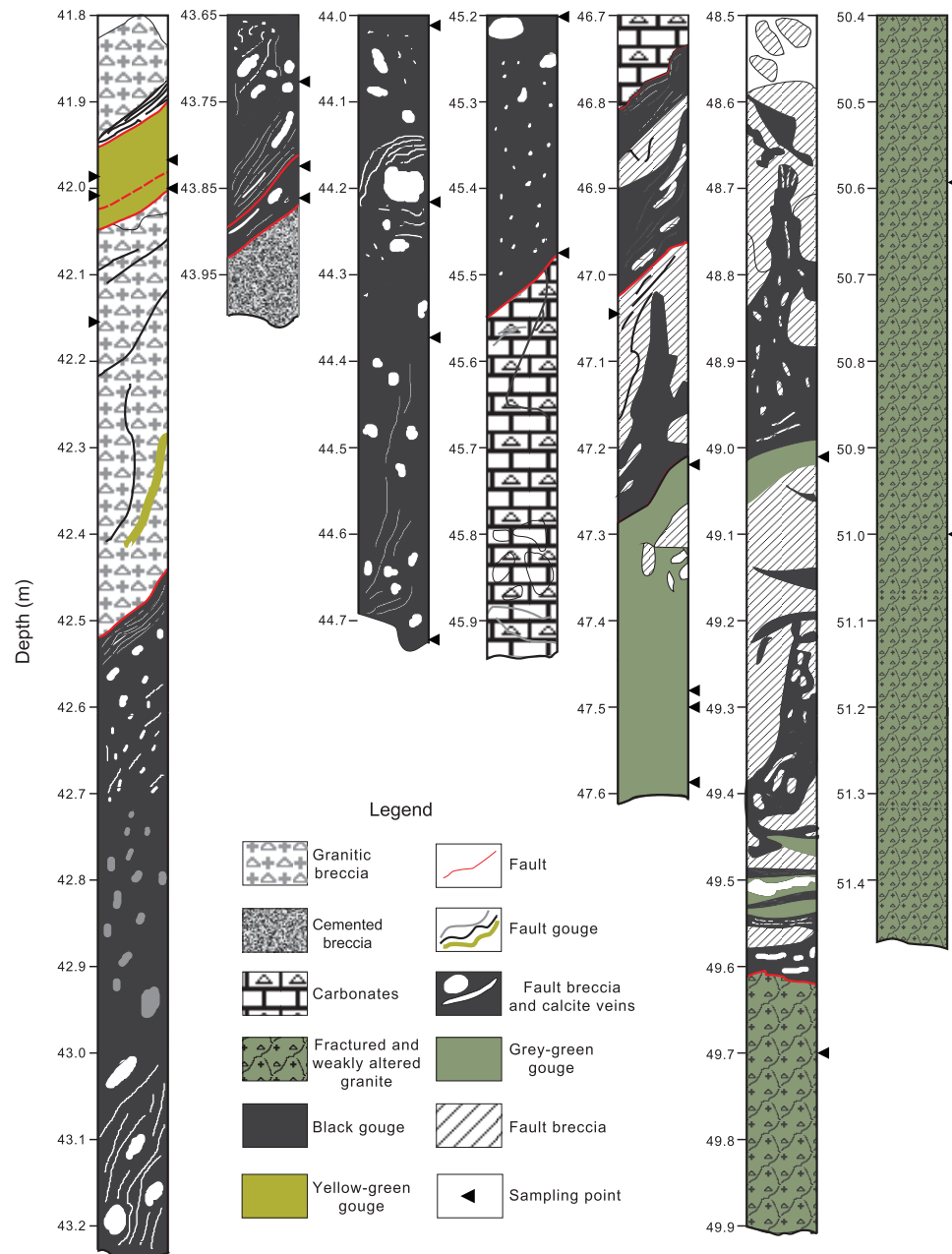
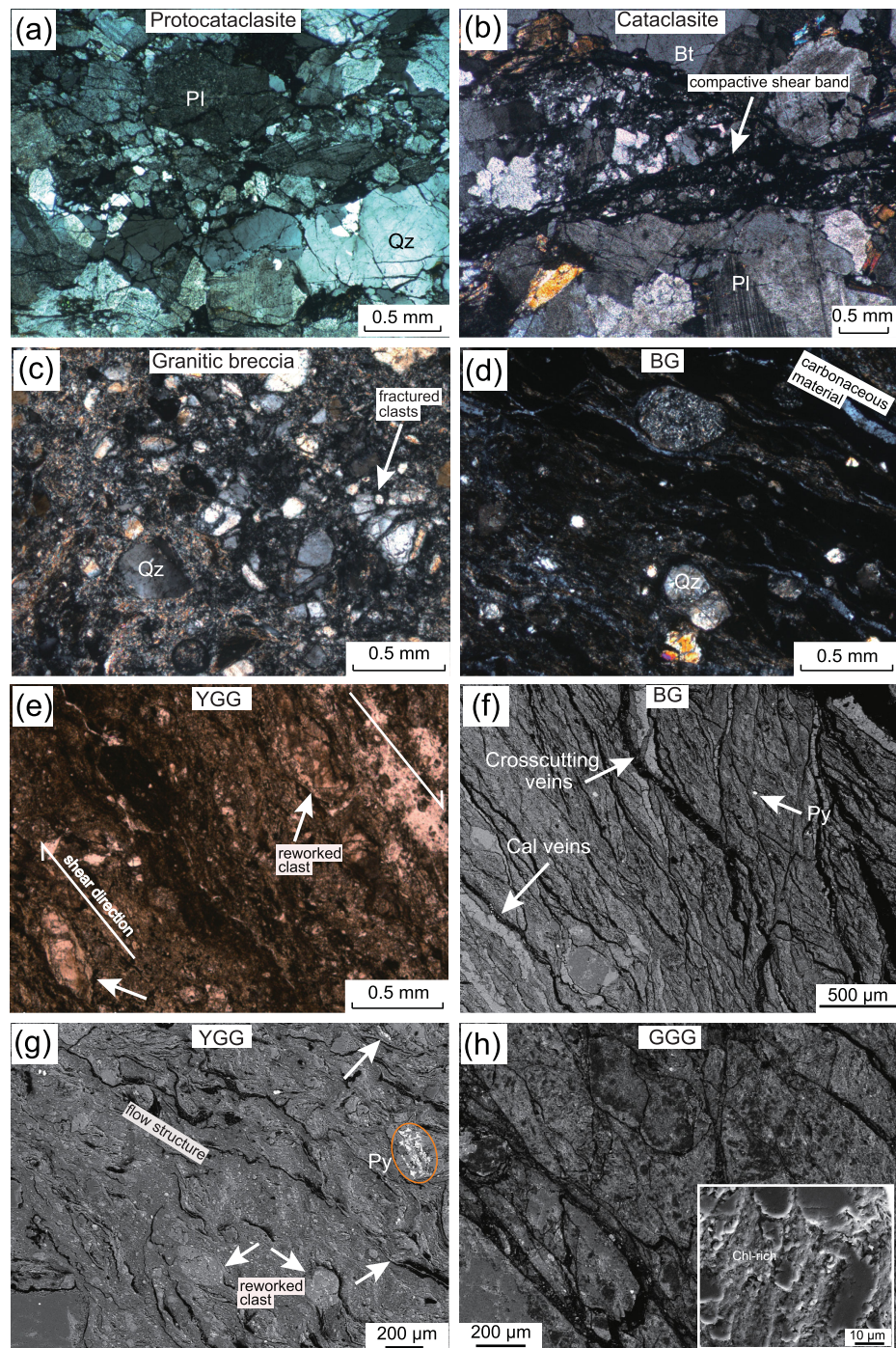


Figure 3. Fault rock distribution in the fault core from 41.8 m to ~51.4 m in Hole B. Triangles mark the sampling points.

that are parallel to the shear plane (Figures 4d and 4f). YGG mainly consists of clay-sized materials, quartz clasts, and a small amount of feldspars; microshear bands and flow structures are discerned (Figure 4e). Reworked grains are widespread in the YGG, and pyrite appears to be locally present as detected with scanning electron microscopy (SEM) (Figure 4g). The GGG generally has similar composition as the YGG, and in contrast the GGG shows a relatively weakly deformed structure, with much less calcite vein material present (Figure 4h).

Overall, a clear increasing trend of grain comminution and fluid alteration is discerned from the (proto-)cataclastite, via the granitic breccia to the fault gouges. The fault gouges, which have accommodated significant displacement in multiple increments of shear, show the highest degree of fracturing and grain comminution. Less shear displacement has been accommodated by the (proto-)cataclastite. However, overprinting by extensive fracturing and precipitation of typical alteration minerals suggest that these rock have



**Figure 4.** Optical microscope images (a–e) and scanning electron micrograph (SEM) images (f–h) of the typical fault rocks. (a) Protocataclasite with high density of cracks, in and along which alterations of minerals occurred. (b) Cataclasite with pervasive mineral alterations and fragmentation. (c) Granitic breccia showing a fragments-embedded-in-matrix texture, with extensive alteration of feldspars to mica and clay minerals. (d) and (f) Black gouge (BG) with multiple episodes of calcite veins and recycled clasts; calcite veins precipitated in the cracks or around the edges of the clasts. (e) and (g) Yellow-green gouge (YGG) consisting of clay-sized matrix and quartz clasts, with microshear bands and flow structures, and presence of pyrite occasionally. (h) Green-grey gouge (GGG) showing a relatively weakly deformed structure, with much less calcite vein material present. Pl, plagioclase; Qz, quartz; Bt, biotite; Cal, calcite; Py, pyrite; Chl, chlorite. (a–d): cross-polarized light, (e); plane-polarized light. (f–h) are backscattered electron images obtained using a Zeiss SIGMA Field-Emission Scanning Electron Microscope (Zeiss, Germany) at operating voltages between 15 and 25 kV.

undergone a complex history, involving both brittle deformation and pervasive fluid-rock interaction. *Duan et al.* [2016] provide a more detailed description of these drill cores, including microstructural, mineralogical, and geochemical characteristics.

In this study, we investigated 58 core samples retrieved from these two holes. Protocataclase and cataclase samples are mainly collected from Hole A. The granitic host rock, granitic breccia, fault gouges (YGG, BG, and GGG), and FWAG are collected from Hole B (the sampling levels are indicated in Figures 2 and 3).

### 3. Methods

Low (976 Hz) and high (15616 Hz) frequency magnetic susceptibilities ( $\chi_{976\text{Hz}}$  and  $\chi_{15616\text{Hz}}$ , respectively, expressed on a mass-specific basis) were measured on bulk samples of a mass ranging between 5 and 10 g with an MFK1-FA Multi-Function Kappabridge susceptometer (AGICO, Brno, Czech Republic) with a detection limit of  $2 \times 10^{-8}$  SI and a measurement accuracy of 0.1%, at a field intensity of 200 A/m (peak-to-peak). Frequency dependence of magnetic susceptibility ( $\chi_{fd}\%$ ) was calculated as  $\chi_{fd}\% = [(\chi_{976\text{Hz}} - \chi_{15616\text{Hz}})/\chi_{976\text{Hz}}] \times 100$ .  $\chi_{976\text{Hz}}$  is taken as the mass-specific low-field magnetic susceptibility ( $\chi_{lf}$ ). An anhysteretic remanent magnetization (ARM) was imparted in a peak alternating field (AF) of 100 mT with a direct current (DC) bias field of 0.05 mT parallel to the AF axis using a Molspin alternating field demagnetizer (Molspin Ltd., UK) with partial ARM attachment. ARMs were measured with a JR-6A spinner magnetometer (AGICO, Brno, Czech Republic) with a sensitivity of  $2 \times 10^{-6}$  A/m. Magnetic hysteresis loops and back-field remanent magnetizations were measured on 0.3–0.5 g powdered samples to determine hysteresis parameters, coercive force ( $B_c$ ), remanence coercivity ( $B_{cr}$ ), saturation remanence ( $M_{rs}$ ), and saturation magnetization ( $M_s$ ) with a MicroMag™ Model 3900 vibrating sample magnetometer (VSM, Princeton Measurements Corp.) with a sensitivity of  $5 \times 10^{-10}$  Am<sup>2</sup> at 1 s per measured point; the maximum applied field was 1.0 T. The high-field magnetic susceptibility ( $\chi_{hf}$ ) was calculated from the high-field slope (above 0.7 T) of each hysteresis loop. The ferrimagnetic contribution ( $\chi_{ferri}$ ) to the magnetic susceptibility is then obtained from  $\chi_{ferri} = \chi_{lf} - \chi_{hf}$ .

Magnetization versus temperature of representative samples was measured in air by a modified horizontal translation type Curie balance, with a sensitivity of approximately  $5 \times 10^{-9}$  Am<sup>2</sup> [Mullender *et al.*, 1993]. Between ~40 and ~70 mg of powdered sample was put into a quartz glass sample holder and held in place by quartz wool; heating and cooling rates were both 10°C/min. Stepwise thermomagnetic runs were carried out with intermittent cooling to 100°C lower than the maximum temperature of each segment. The maximum temperatures of the successive heating segments were 150, 250, 400, 520, 620, and 700°C, respectively.

XRD analysis for relative mineral content (in weight percent, wt %) including semiquantitative analysis of clay minerals was performed with a Rigaku D/MAX 2400 12 kW X-Ray diffractometer (Cu K $\alpha$  radiation (0.15418 nm), 45 kV and 100 mA), with a detection limit of ~1 wt % for major phases. Unoriented, powdered bulk samples were scanned in the range from 3° to 45° 2 $\theta$  with a step size of 0.02° at a scan rate of 2°/min. The relative clay amounts in the bulk sample were evaluated first; the clay mineralogy was further specified through analysis of the clay-sized fraction (< 2  $\mu\text{m}$ ) which was separated by the sedimentation method. The clay-water slurry was air-dried on glass slides and ethylene glycol was added to detect the swelling components (smectite or illite/smectite mixed layer clay minerals). Then the samples were heated to 550°C to distinguish kaolinite from chlorite [Lin *et al.*, 1992].

Crushed and milled powder samples with grain size < 200 mesh were used to determine the concentrations (in wt %) of major and minor elements (including SiO<sub>2</sub>, Al<sub>2</sub>O<sub>3</sub>, total Fe calculated as Fe<sub>2</sub>O<sub>3</sub><sup>T</sup>, K<sub>2</sub>O, MnO, MgO, CaO, Na<sub>2</sub>O, TiO<sub>2</sub>, and P<sub>2</sub>O<sub>5</sub>) using a Philips MagiX-PRO 2440 X-ray fluorescence (XRF) spectrometer. Duplicate and standard analyses were carried out to ensure that accuracy and precision were within acceptable limits. Analytical reproducibility for most oxides was less than 2% relative error, except for Na<sub>2</sub>O with an error of about 5%. The ferrous iron content (calculated as FeO) was determined by titration using K<sub>2</sub>Cr<sub>2</sub>O<sub>7</sub> after being digested by a H<sub>2</sub>SO<sub>4</sub>+HF mixture [Rao and Govil, 1995], and ferric iron, calculated as Fe<sub>2</sub>O<sub>3</sub>, was then obtained by subtracting the FeO from total iron (Fe<sub>2</sub>O<sub>3</sub><sup>T</sup>) obtained by XRF,  $\text{Fe}_2\text{O}_3 = \text{Fe}_2\text{O}_3^{\text{T}} - \text{FeO} \times 1.111$ . The volatile components were measured by thermogravimetric methodology developed by Tanaka *et al.* [2001]: water (presented as "H<sub>2</sub>O<sup>+</sup>") was determined by heating the samples at 110°C in a closed vial connected to a chamber with a 100% sulfuric acid solution. The sulfuric acid solution absorbs the evaporating water; the related weight increase is recorded. Weight loss after ignition of the sample at 1000°C for 3 h

was measured and expressed as a percentage; it is the loss on ignition (LOI). CO<sub>2</sub> contents (in wt %) were measured with a non-aqueous titration method for the determination of total dissolved carbon dioxide [Johnson *et al.*, 1985], in which CO<sub>2</sub> is measured coulometrically by the quantity of electricity (coulombs) consumed to electrogenerate OH<sup>-</sup> ions for the titration of the acid formed by the reaction of CO<sub>2</sub> and ethanolamine.

To quantify the element transfer and volume (or mass) loss or gain within the fault zone, bulk rock volume losses/gains of the fault rocks relative to the host rock were estimated using the isocon method of geochemical mass balance [Grant, 1986; Tanaka *et al.*, 2001]. This approach is used to determine the mobility degree of elements by plotting element concentrations in an altered sample (or the mean of a group of altered samples) against an unaltered reference precursor, in a "Grant-type plot" [Grant, 1986]. The hardly mobile or completely immobile elements during fluid-rock interaction processes (so-called high field strength (HFS) elements) should be distributed along a straight line passing through the origin (i.e., the "isocon line"). Elements plotting above or below this line are enriched and depleted, respectively. The slope of this isocon line ( $S$ ) defines the net mass change in per cent ( $\Delta M$ ) of the altered sample(s),  $\Delta M = [(1/S) - 1] \times 100$  [Grant, 1986]. TiO<sub>2</sub> was chosen as the immobile oxide [e.g., Tanaka *et al.*, 2001; Chen *et al.*, 2007; Chen *et al.*, 2013]. Here we use the term "mass loss," which is almost equivalent to "volume loss," because reasonable estimates of density differences between host and fault rocks are within  $\pm 5\%$  [Goddard and Evans, 1995].

## 4. Results

### 4.1. Magnetic Susceptibilities

Magnetic parameters of the drill core samples are plotted against depth in Figure 5 and summarized in Table 1. The host rock (granite) shows a distinctly variable  $\chi_{lf}$  (from 5.38 to  $68.45 \times 10^{-8} \text{ m}^3 \text{ kg}^{-1}$ ) with an average ( $\bar{x}$ )  $\pm$  standard deviation of  $33.84 \pm 25.09 \times 10^{-8} \text{ m}^3 \text{ kg}^{-1}$  ( $n = 8$ ), followed in decreasing order by  $\chi_{lf}$  of the granitic breccia ( $\bar{x} = 13.08 \pm 5.49 \times 10^{-8} \text{ m}^3 \text{ kg}^{-1}$ ,  $n = 7$ ), the FWAG ( $\bar{x} = 5.74 \pm 1.65 \times 10^{-8} \text{ m}^3 \text{ kg}^{-1}$ ,  $n = 7$ ), the protocataclasite ( $\bar{x} = 4.03 \pm 0.90 \times 10^{-8} \text{ m}^3 \text{ kg}^{-1}$ ,  $n = 6$ ), and the cataclasite ( $\bar{x} = 3.58 \pm 0.78 \times 10^{-8} \text{ m}^3 \text{ kg}^{-1}$ ,  $n = 11$ ) (Table 1). Within the gouge zones, the YGG group has the highest  $\chi_{lf}$  with an average value of  $32.69 \pm 2.19 \times 10^{-8} \text{ m}^3 \text{ kg}^{-1}$  ( $n = 4$ ), followed by the GGG group with an average  $\chi_{lf}$  of  $31.06 \pm 4.78 \times 10^{-8} \text{ m}^3 \text{ kg}^{-1}$  ( $n = 5$ ), while the BG group displays the lowest average  $\chi_{lf}$  ( $7.96 \pm 4.34 \times 10^{-8} \text{ m}^3 \text{ kg}^{-1}$ ,  $n = 10$ ).

The host rock has a low average  $\chi_{hf}$  ( $2.77 \pm 0.51 \times 10^{-8} \text{ m}^3 \text{ kg}^{-1}$ ). Granitic breccia, FWAG, protocataclasite, and cataclasite generally have much higher  $\chi_{hf}$ ;  $\chi_{ferri}$  is therefore lower (Table 1). Within the gouge zones, GGG group has the highest  $\chi_{hf}$  ( $29.21 \pm 4.25 \times 10^{-8} \text{ m}^3 \text{ kg}^{-1}$ ), followed downwards by the YGG ( $26.75 \pm 3.79 \times 10^{-8} \text{ m}^3 \text{ kg}^{-1}$ ) and BG ( $6.32 \pm 3.90 \times 10^{-8} \text{ m}^3 \text{ kg}^{-1}$ ) groups.

$\chi_{fd}\%$  values of the host rock are lowest (average ( $\bar{x}$ ):  $2.61 \pm 1.17\%$ ,  $n = 8$ ), followed in increasing order by those of the granitic breccia ( $\bar{x} = 2.80 \pm 0.60\%$ ,  $n = 7$ ), the FWAG ( $\bar{x} = 3.15 \pm 0.26\%$ ,  $n = 7$ ), the protocataclasite ( $\bar{x} = 4.74 \pm 1.58\%$ ,  $n = 6$ ), and finally the cataclasite ( $\bar{x} = 6.57 \pm 1.53\%$ ,  $n = 11$ ) (Table 1). The gouge zones, noteworthy, have much lower  $\chi_{fd}\%$  than the (proto-)cataclasite. The YGG has an average  $\chi_{fd}\%$  value of  $2.19 \pm 0.15\%$  ( $n = 4$ ); the GGG has  $\bar{x} = 2.07 \pm 0.19\%$  ( $n = 5$ ). The BG has a slightly higher  $\chi_{fd}\%$  with an average value of  $3.36 \pm 1.95\%$  ( $n = 10$ ).

### 4.2. Thermomagnetic Analysis

Heating curves of host rocks, granitic breccia, FWAG, protocataclasite, and cataclasite show a monotonous decay in magnetization from room temperature until approximately 580°C (Figures 6a–6e), which is typical for magnetite [Dunlop and Özdemir, 1997]. In most of the gouge samples, the heating curves show a hyperbolic decay from room temperature until approximately 450°C, at which point the magnetization starts to increase and peaks at approximately 500°C (Figures 6e, 6g–6i). This is consistent with the oxidation of iron sulfides, like pyrite, identified by microscopic observations (Figure 4) and detected by XRD analysis (see section 4.5), resulting in the creation of a new ferrimagnetic phase. After this peak, the magnetization decays linearly until approximately 580–600°C, indicating the presence of magnetite. In addition, a more rapid decay in magnetization between  $\sim 250$  and  $\sim 500^\circ\text{C}$  is observed on the heating curve for one of the YGG samples (D3s-35, Figure 6g). It may be linked to the oxidation of existing very fine-grained magnetite. On the cooling curves of host rocks, granitic breccia, protocataclasite, and cataclasite, the magnetization is

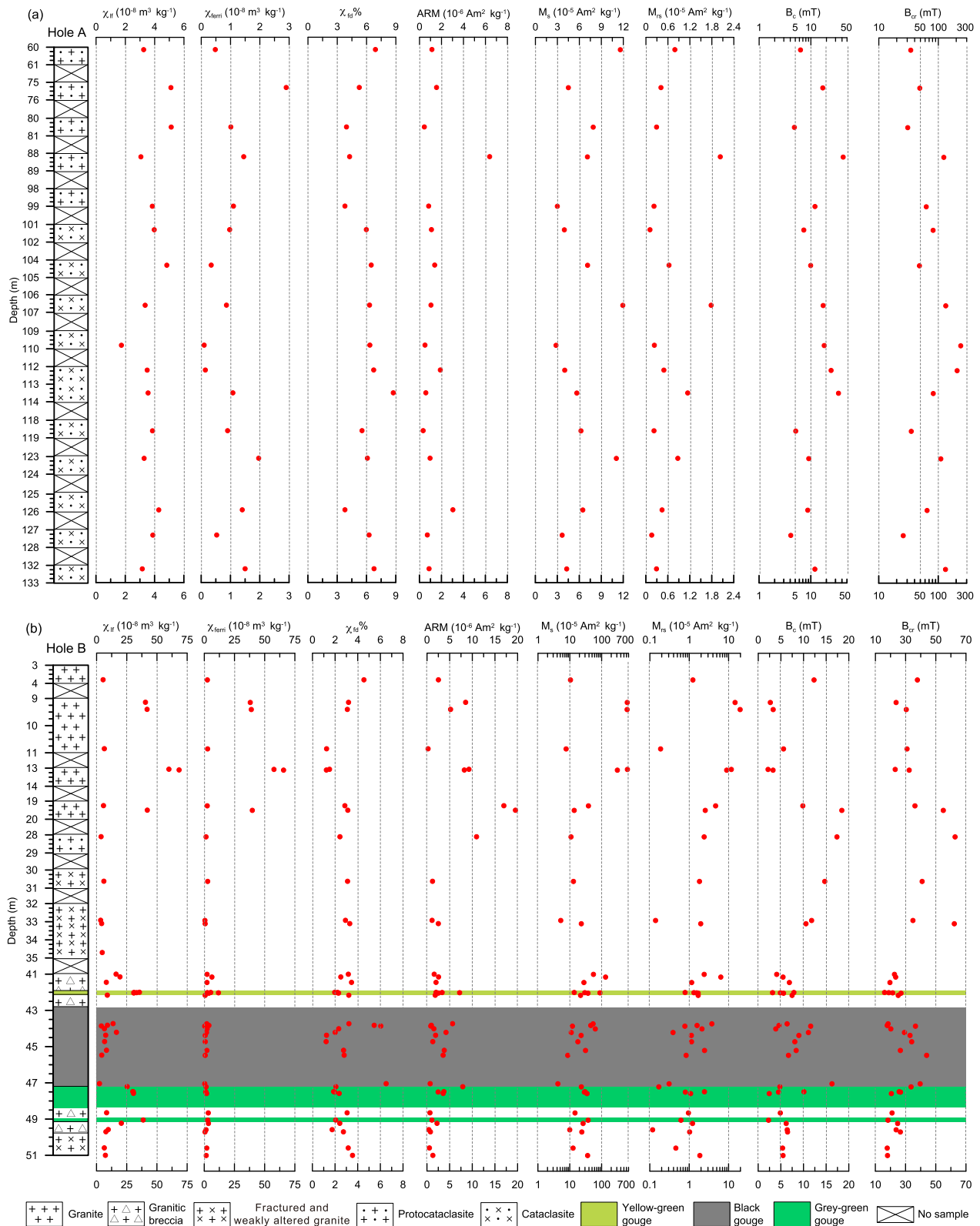


**Figure 5.** Downhole magnetic parameters of core samples from (a) Hole A and (b) Hole B. Note the depth scale; the crosses in the stratigraphic columns indicate that there is no sample from the corresponding intervals. (left to right) Lithological unit allocation, mass-specific low-field magnetic susceptibility ( $\chi_{lf}$ ), ferrimagnetic contribution of magnetic susceptibility ( $\chi_{ferrim}$ ), frequency-dependent magnetic susceptibility ( $\chi_{fd}\%$ ), anhysteretic remanent magnetization (ARM), saturation magnetization ( $M_s$ ), saturation remanence ( $M_r$ ), coercive force ( $B_c$ ), and remanent coercive force ( $B_{cr}$ ). Note: Frequency-dependent magnetic susceptibilities were measured at two frequencies, 976 (low) and 15,616 Hz (high), with a MFK1-FA Kappabridge susceptometer; thus, here  $\chi_{fd}\%$  is 1.6 times that obtained with a Bartington MS2B sensor, which operates at 465 Hz (low frequency) and 4650 Hz (high frequency).

**Table 1.** Summary of Magnetic Parameters of Drill Core Samples From the LMFD-3 Holes at the Jinhe Site on the Yingxiu-Beichuan Fault<sup>a</sup>

Samples	$\chi_{lf}$ ( $10^{-8} \text{ m}^3 \text{ kg}^{-1}$ )	$\chi_{hf}$ ( $10^{-8} \text{ m}^3 \text{ kg}^{-1}$ )	$\chi_{ferri}$ ( $10^{-8} \text{ m}^3 \text{ kg}^{-1}$ )	$\chi_{fd}$ (%)	ARM ( $10^{-6} \text{ Am}^2 \text{ kg}^{-1}$ )	$M_s$ ( $10^{-5} \text{ Am}^2 \text{ kg}^{-1}$ )	$M_{rs}$ ( $10^{-5} \text{ Am}^2 \text{ kg}^{-1}$ )	$B_c$ (mT)	$B_{cr}$ (mT)
Host rock (n = 8)	5.38–68.45 33.84 ± 25.09	2.19–3.66 2.77 ± 0.51	2.50–65.77 31.07 ± 25.45	1.24–4.55 2.61 ± 1.17	0.27–19.54 8.83 ± 6.63	7.73–651.05 289.86 ± 310.44	0.19–19.81 8.01 ± 7.05	2.2–18.5 7.2 ± 5.8	23.2–55.0 33.8 ± 10.0
FWAG (n = 7)	3.42–7.81 5.74 ± 1.65	2.83–7.11 4.52 ± 1.53	0.59–2.86 1.47 ± 0.93	2.74–3.55 3.15 ± 0.26	0.56–2.86 1.48 ± 0.87	5.22–36.47 17.52 ± 0.92	0.14–1.97 1.09 ± 0.79	5.4–14.7 8.8 ± 3.6	17.9–62.3 33.6 ± 15.4
Fault breccia (n = 7)	8.16–20.59 13.08 ± 5.49	5.01–17.04 10.15 ± 4.52	0.83–6.41 2.93 ± 1.81	1.75–3.46 2.80 ± 0.60	0.44–2.58 1.63 ± 0.79	10.03–133.86 41.49 ± 43.28	0.12–6.37 1.99 ± 2.05	4.1–7.5 5.9 ± 1.2	19.7–25.2 23.0 ± 2.0
Protocataclasite (n = 6)	3.06–5.13 4.03 ± 0.90	1.61–4.12 2.62 ± 0.85	0.48–2.90 1.41 ± 0.82	2.43–6.91 4.74 ± 1.58	0.44–10.95 3.55 ± 4.24	2.99–11.59 7.51 ± 3.42	0.22–2.40 1.02 ± 0.95	4.8–42.1 16.6 ± 13.6	30.6–123.6 60.5 ± 33.8
Cataclasite (n = 11)	1.73–4.83 3.58 ± 0.78	1.32–4.49 2.69 ± 0.92	0.10–1.96 0.89 ± 0.59	3.79–9.60 6.57 ± 1.53	0.33–3.03 1.13 ± 0.77	2.81–11.93 6.10 ± 2.98	0.11–1.78 0.58 ± 0.51	4.1–34.2 13.7 ± 9.2	25.8–237.9 105.3 ± 68.4
YGG (n = 4)	30.92–35.57 32.69 ± 2.19	21.40–30.13 26.75 ± 3.79	2.61–11.82 5.94 ± 4.09	1.97–2.32 2.19 ± 0.15	2.02–7.22 3.79 ± 2.35	13.87–88.95 42.52 ± 32.48	0.79–1.69 1.34 ± 0.40	3.2–7.9 5.4 ± 2.0	16.1–27.0 20.9 ± 4.6
BG (n = 10)	2.51–16.53 7.96 ± 4.34	2.02–14.58 6.32 ± 3.90	0.46–3.92 1.64 ± 1.11	1.22–6.52 3.36 ± 1.95	0.72–5.66 2.46 ± 1.72	4.26–63.48 27.21 ± 20.73	0.31–3.78 1.46 ± 1.07	3.9–16.3 8.6 ± 3.7	17.9–44.0 30.0 ± 9.1
GGG (n = 5)	25.43–38.69 31.06 ± 4.78	23.83–35.74 29.21 ± 4.25	1.26–2.95 1.85 ± 0.68	1.88–2.37 2.07 ± 0.19	1.10–7.92 3.77 ± 2.55	23.20–37.89 31.06 ± 5.69	0.17–2.45 1.03 ± 0.86	2.3–10.1 4.8 ± 3.2	18.4–33.7 25.0 ± 5.9

<sup>a</sup>Note:  $\chi_{lf}$ , mass-specific low-field magnetic susceptibility;  $\chi_{hf}$ , mass-specific high-field magnetic susceptibility;  $\chi_{ferri}$ , the ferrimagnetic contribution to the magnetic susceptibility,  $\chi_{ferri} = \chi_{lf} - \chi_{hf}$ ;  $\chi_{fd}$ %, frequency dependence of magnetic susceptibility; ARM, anhysteretic remanent magnetization;  $M_s$ , saturation remanence;  $M_{rs}$ , saturation magnetization;  $B_c$ , coercive force;  $B_{cr}$ , remanence coercivity. The statistical results of different parameters are given as minimum – maximum, average ± standard deviation. FWAG, fractured and weakly altered granite; YGG, yellow-green-gouge; BG, black-gouge; GGG, grey-green-gouge.

distinctly increasing below 580–520°C resulting in cooling curves above the corresponding heating curves (Figures 6a–6d). This indicates that traces of magnetite are newly formed in the samples. However, for most of the fault gouge and FWAG samples, the cooling curves continue to show paramagnetic behavior (i.e., hyperbolic shape) below the corresponding heating curves (Figures 6e–6i), suggesting that the traces of fine-grained magnetite in these samples have been (mostly) thermochemically removed during the heating.

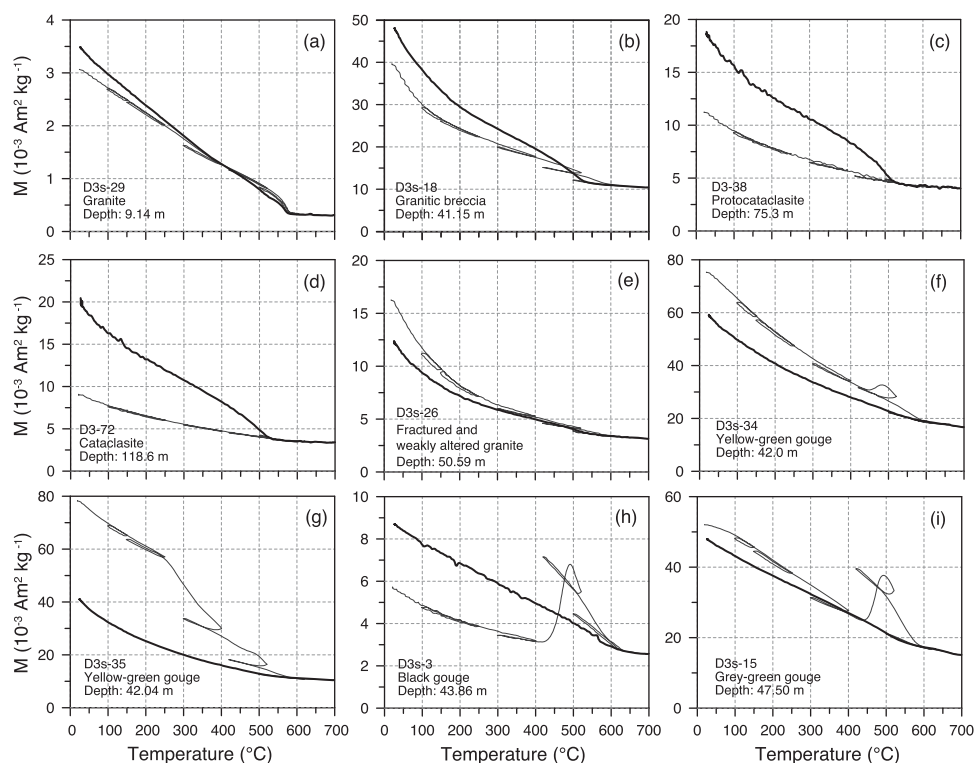


**Figure 6.** Stepwise thermomagnetic analyses of selected drill core samples performed with a modified horizontal translation Curie balance [Mullender *et al.*, 1993]. Heating/cooling rates are 10°C/min; the magnetic field was cycled between 100 and 300 mT. Heating (cooling) segments are indicated with thin (thick) lines.

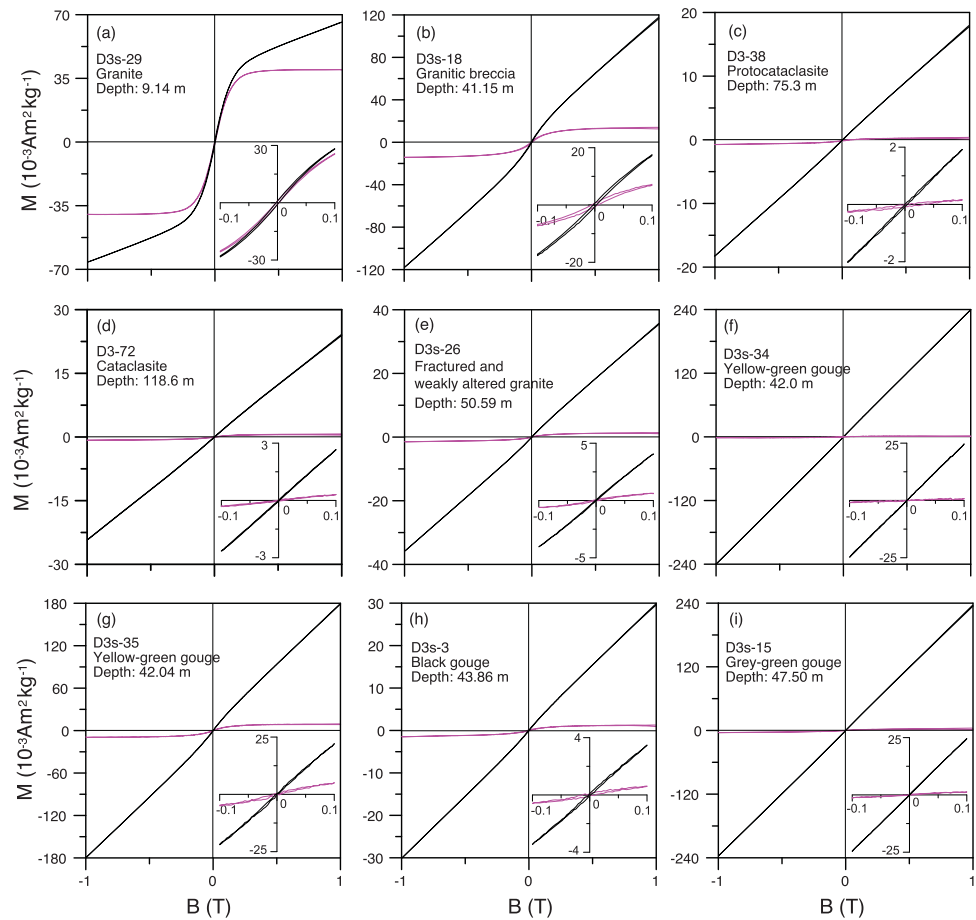


**Figure 7.** Magnetic hysteresis loops for selected core samples before (black) and after (magenta) para-/diamagnetic correction, where B is the applied magnetic field, and M is the magnetization. “D3” or “D3s” in sample numbers indicate that the corresponding sample is collected from Hole A or Hole B, respectively. Insets show close-up views of the central parts of the hysteresis loops ( $\pm 0.1$  T).

### 4.3. Magnetic Hysteresis Properties

A low-coercivity ferrimagnetic component is the dominant magnetic carrier in the host rock (Figure 7a).  $M_s$  (average:  $289.86 \pm 310.44 \times 10^{-5} \text{ Am}^2 \text{ kg}^{-1}$ ,  $n = 8$ ) and  $M_{rs}$  (average:  $8.01 \pm 7.05 \times 10^{-5} \text{ Am}^2 \text{ kg}^{-1}$ ,  $n = 8$ ) values are variable, and follow a similar trend as  $\chi_{if}$  values (Table 1). In contrast, granitic breccia is dominantly paramagnetic, characterized by a uniform magnetization versus magnetizing field slope (Figure 7b); only minor hysteresis closing below  $\sim 0.3$  T is observed. Protocataclasite, cataclasite, and FWAG appear to be almost entirely paramagnetic (Figures 7c–7e).  $M_s$  and  $M_{rs}$  values decrease significantly from host rock to granitic breccia (average  $M_s$ :  $41.49 \pm 43.28 \times 10^{-5} \text{ Am}^2 \text{ kg}^{-1}$ , average  $M_{rs}$ :  $1.99 \pm 2.05 \times 10^{-5} \text{ Am}^2 \text{ kg}^{-1}$ ,  $n = 7$ ), FWAG (average  $M_s$ :  $17.52 \pm 0.92 \times 10^{-5} \text{ Am}^2 \text{ kg}^{-1}$ , average  $M_{rs}$ :  $1.09 \pm 0.79 \times 10^{-5} \text{ Am}^2 \text{ kg}^{-1}$ ,  $n = 7$ ), protocataclasite (average  $M_s$ :  $7.51 \pm 3.42 \times 10^{-5} \text{ Am}^2 \text{ kg}^{-1}$ , average  $M_{rs}$ :  $1.02 \pm 0.95 \times 10^{-5} \text{ Am}^2 \text{ kg}^{-1}$ ,  $n = 6$ ), and cataclasite (average  $M_s$ :  $6.10 \pm 2.98 \times 10^{-5} \text{ Am}^2 \text{ kg}^{-1}$ , average  $M_{rs}$ :  $0.58 \pm 0.51 \times 10^{-5} \text{ Am}^2 \text{ kg}^{-1}$ ,  $n = 11$ ).

The host rock has an average  $B_c$  of  $7.2 \pm 5.8$  mT and  $B_{cr}$  of  $33.8 \pm 10.0$  mT, respectively. Granitic breccia has lower  $B_c$  (average:  $5.9 \pm 1.2$  mT) and  $B_{cr}$  values (average:  $23.0 \pm 2.0$  mT). The trends in  $B_c$  and  $B_{cr}$  are the same as in  $M_s$  and  $M_{rs}$ . However, for the more altered rocks—the FWAG, protocataclasite, and cataclasite— $B_c$  (averages of  $8.8 \pm 3.6$  mT for FWAG,  $16.6 \pm 13.6$  mT for protocataclasite, and  $13.7 \pm 9.2$  mT for cataclasite) and  $B_{cr}$  trends (averages of  $33.6 \pm 15.4$  mT for FWAG,  $60.5 \pm 33.8$  mT for protocataclasite, and  $105.3 \pm 68.4$  mT for cataclasite) are generally opposite to the trends in  $M_s$  and  $M_{rs}$  (Table 1).

As is observed for FAWG and (proto-)cataclasite, all fault gouge samples are also essentially paramagnetic (Figures 7f–7i). The YGG group has the highest but most variable  $M_s$  (average:  $42.52 \pm 32.48 \times 10^{-5} \text{ Am}^2$

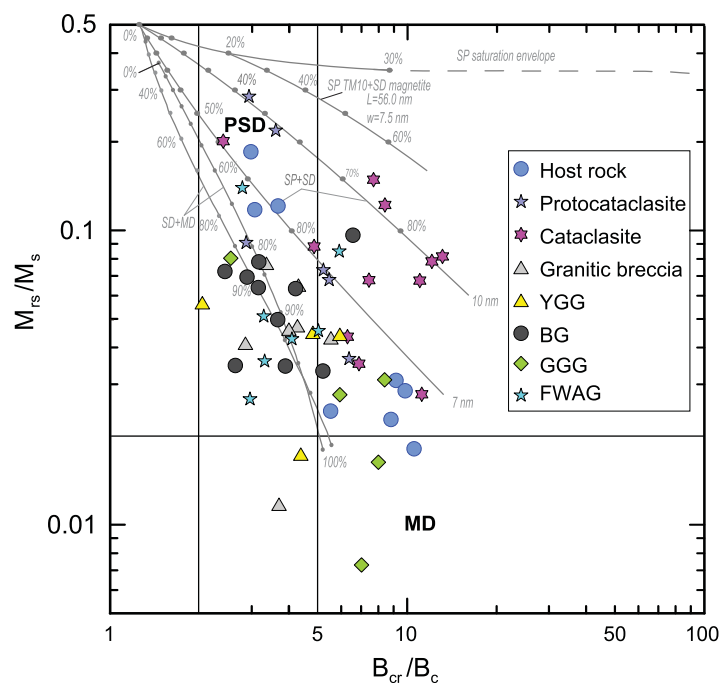


**Figure 8.** Day plot of the hysteresis ratios  $M_{rs}/M_s$  and  $B_{cr}/B_c$  of all 58 drill core samples. Single-domain (SD), pseudo-single-domain (PSD), and multidomain (MD) boundaries are after Dunlop [2002]. Numbers adjacent to curves are volume fractions of the soft component (superparamagnetic, SP or MD) in mixtures with SD grains. FWAG, fractured and weakly altered granite; YGG, yellow-green-gouge; BG, black-gouge; GGG, grey-green-gouge.

$\text{kg}^{-1}$ ), while its  $M_{rs}$  and  $B_c$  values are (averages:  $1.34 \pm 0.40 \times 10^{-5} \text{ Am}^2 \text{ kg}^{-1}$  and  $5.4 \pm 2.0 \text{ mT}$  respectively). Its  $B_{cr}$  values are lowest from all gouges (average:  $20.9 \pm 4.6 \text{ mT}$ ). The BG group has the highest  $B_c$  (average:  $8.6 \pm 3.7 \text{ mT}$ ) and  $B_{cr}$  (average:  $30.0 \pm 9.1 \text{ mT}$ ) values, and the lowest  $M_s$  (average:  $27.21 \pm 20.73 \times 10^{-5} \text{ Am}^2 \text{ kg}^{-1}$ ), although it has the highest  $M_{rs}$  (average:  $1.46 \pm 1.07 \times 10^{-5} \text{ Am}^2 \text{ kg}^{-1}$ ).

The hysteresis data ( $M_{rs}/M_s$  and  $B_{cr}/B_c$ ) of all samples are summarized in a Day plot (Figure 8) [Day *et al.*, 1977; Dunlop, 2002]. It is seen that most of the host rock and GGG samples plot in the multidomain (MD) region. Granitic breccia, FWAG, YGG samples, and most of BG samples are located in the pseudo-single domain (PSD) range. Most of protocataclasite and cataclasite are distributed along the superparamagnetic (SP, 7 nm) + single domain (SD) and SP(10 nm) + SD mixing curves.

Overall, the magnetic properties of granitic host rock are dominated by small MD magnetite particles. The main magnetic carrier identified for the ferrimagnetic fraction in all fault rock types is magnetite as well. The extremely low proportions of ferrimagnetic phases confirm that their magnetic properties (e.g., magnetic susceptibility, hysteresis loops, and thermomagnetic behavior) are essentially controlled by the paramagnetic fraction. These trace amounts of magnetite are inferred to be PSD for granitic breccia, protocataclasite, cataclasite, FWAG, and most of the fault gouge samples, except for the GGG samples where it shows up in the MD range. Noteworthy, a significant amount of SP particles is present in the protocataclasite and cataclasite samples, emerging from their plotting on the Day plot (Figure 8) and also evidenced by their higher  $\chi_{fd}\%$  values (Table 1) [Deearing *et al.*, 1996]. The magnetite concentration exhibits a decreasing trend from host rock, granitic breccia, FWAG, protocataclasite, and cataclasite, as demonstrated by the decreasing values of  $M_s$  and  $\chi_{ferri}$  (Table 1).

#### 4.4. Anhyseretic Remanent Magnetization (ARM)

ARM shows a trend similar to those of  $M_s$  and  $M_{rs}$  for all rock types except the protocataclasite. It decreases from the host rock (average:  $8.83 \pm 6.63 \times 10^{-6} \text{ Am}^2 \text{ kg}^{-1}$ ,  $n = 8$ ), via granitic breccia (average:  $1.63 \pm 0.79 \times 10^{-6} \text{ Am}^2 \text{ kg}^{-1}$ ,  $n = 7$ ), FWAG (average:  $1.48 \pm 0.87 \times 10^{-6} \text{ Am}^2 \text{ kg}^{-1}$ ,  $n = 7$ ), and cataclasite (average:  $1.13 \pm 0.77 \times 10^{-6} \text{ Am}^2 \text{ kg}^{-1}$ ,  $n = 11$ ) (Table 1), although distributions overlap by a fair amount. The protocataclasite has higher and more variable ARM values (average:  $3.55 \pm 4.24 \times 10^{-6} \text{ Am}^2 \text{ kg}^{-1}$ ,  $n = 6$ ). ARM of the YGG group (average:  $3.79 \pm 2.35 \times 10^{-6} \text{ Am}^2 \text{ kg}^{-1}$ ,  $n = 4$ ) is comparable to that of the GGG group (average:  $3.77 \pm 2.55 \times 10^{-6} \text{ Am}^2 \text{ kg}^{-1}$ ,  $n = 5$ ), while the BG group has lower ARM values (average:  $2.46 \pm 1.72 \times 10^{-6} \text{ Am}^2 \text{ kg}^{-1}$ ,  $n = 10$ ) (Table 1).

#### 4.5. Mineral Assemblages

XRD analyses were performed on 29 drill core samples. Marked differences in bulk mineralogy and clay minerals (in the clay-sized fraction) are observed in the host rocks and the various types of fault rocks (Figure 9). The host rock predominantly consists of feldspars (64 wt %) and quartz (29 wt %). Mineral assemblages are

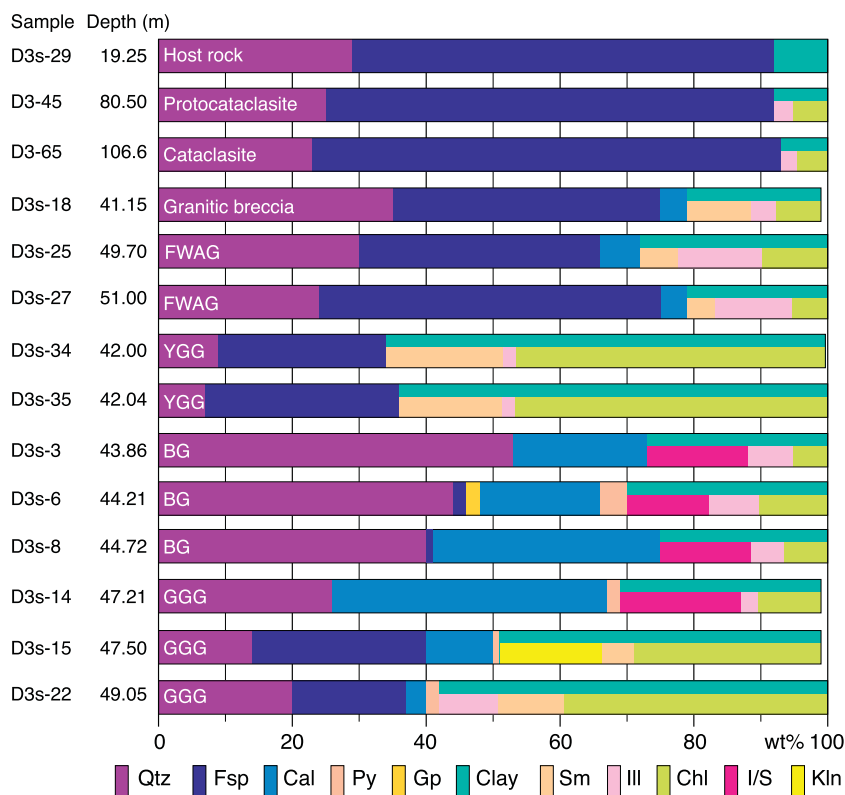


**Figure 9.** Mineralogical assemblages of representative drill core samples from the LMFD-3 holes. Qtz, quartz; Fsp, feldspar; Cal, calcite; Py, pyrite; Gp, gypsum; Clay, Clay fraction; Sm, smectite; Ill, illite; Chl, Chlorite; I/S, mixed-layer illite/smectite; Kln, kaolinite. The reader is referred to section 3 in the main text for details about the analytical procedures for the determination of bulk and clay minerals. FWAG, fractured and weakly altered granite; YGG, yellow-green-gouge; BG, black-gouge; GGG, grey-green-gouge.

similar in the protocataclasite and cataclasite, but minor clay minerals (~8 wt %) are present. With respect to them, granitic breccia is enriched in clay minerals (16–33 wt %) and slightly enriched in quartz (35–37 wt %) and, but depleted in feldspar (40–47 wt %). FWAG shows similar mineral distribution patterns, although relatively higher depletion in feldspar (32–36 wt%; one sample has 52 wt %), and enrichment of clay minerals (21–28 wt %) are observed. Within the fault gouge zones, the YGG group has the lowest abundance of quartz (7–9 wt %), and is the most enriched in clay minerals (~65%). The BG group has the highest content of quartz (40–53 wt %) and shows most depletion in feldspar (1–4 wt %, and undetected in almost half of all samples). Further, it is enriched in calcite (17–49 wt %), while its clay mineral content is moderate (17–37 wt %). The GGG group has a heterogeneous content of calcite (3–41 wt %) and feldspar (17–39 wt %, and below the detection limit in one sample), with a moderate content of quartz (14–26 wt %) and a rather high proportion of clay minerals (30–58 wt %).

The clay fraction of the granitic breccia is generally dominated by variable smectite (7–59 wt %), chlorite (17–42 wt %), and illite (19–68 wt %). In contrast, the clay fraction in the FWAG is higher and dominated by illite (45–63 wt %), followed by chlorite (22–35 wt %), while smectite is minor (15–20 wt %). Concerning the fault gouges, the YGG group is dominated by abundant chlorite (71–73 wt %) with moderate smectite (24–27 wt %) and rather minute amounts of illite (~3 wt %) (Figure 9). The BG group has a much higher content of mixed-layered illite-smectite (I/S) (45–72 wt%), substantial illite (~20 wt%) compared to the YGG gouges, and the lowest content of chlorite (17–39 wt %) of all groups. There is no detectable smectite in the BG group. The GGG group has a moderate content of chlorite (31–68 wt %), minor smectite (10–17 wt %; undetected in one sample) and illite (9–15 wt%, and undetected in most samples), with the occasional presence of I/S and kaolinite.

#### 4.6. Chemical Compositions

Chemical compositions of 45 analyzed samples are summarized in Table 2. With respect to host rock, FWAG, protocataclasite, and cataclasite, granitic breccia has lower contents of Na<sub>2</sub>O and SiO<sub>2</sub>, and higher

contents of MgO and TiO<sub>2</sub>. Generally, MgO, P<sub>2</sub>O<sub>5</sub>, CaO, TiO<sub>2</sub>, Fe<sub>2</sub>O<sub>3</sub>, and FeO are enriched but heterogeneously distributed within the fault gouge zones (Table 2), whereas Na<sub>2</sub>O, Al<sub>2</sub>O<sub>3</sub>, and SiO<sub>2</sub> behave in an opposite sense. More specifically, the YGG group has the highest enrichments in MgO, P<sub>2</sub>O<sub>5</sub>, and TiO<sub>2</sub>, with moderately enriched MnO, FeO, and Fe<sub>2</sub>O<sub>3</sub>; it is moderately depleted in SiO<sub>2</sub> and K<sub>2</sub>O. The BG group has the highest depletion in Na<sub>2</sub>O, the highest enrichment in CaO, and the lowest enrichment in MgO, P<sub>2</sub>O<sub>5</sub>, TiO<sub>2</sub>, Fe<sub>2</sub>O<sub>3</sub>, and FeO. In contrast, the GGG group shows the highest enrichment in MnO, FeO, and Fe<sub>2</sub>O<sub>3</sub>, and moderate enrichment in MgO, P<sub>2</sub>O<sub>5</sub>, and TiO<sub>2</sub>, accompanied by the lowest depletion of SiO<sub>2</sub> and K<sub>2</sub>O (Table 2). Volatile contents (H<sub>2</sub>O<sup>+</sup>, LOI, and CO<sub>2</sub>) are increased several times to several orders of magnitude in the fault gouge zones in comparison to the host rocks. The BG group has the highest LOI and CO<sub>2</sub>, as well as lowest H<sub>2</sub>O<sup>+</sup>. The GGG group has medium H<sub>2</sub>O<sup>+</sup>, CO<sub>2</sub>, and LOI. Accordingly, the YGG group has the highest H<sub>2</sub>O<sup>+</sup>, and lowest CO<sub>2</sub> and LOI (Table 2).

Isocon analysis reveals an increasing trend of mass-loss with respect to the host rock when approaching the fault zone. Rather different mass-losses are observed in the granitic breccia (45.6%), (proto-)cataclasite (10.7%), FWAG (26.5%), YGG (91.5%), BG (67.5%), and GGG (91.2%), respectively (Figure 10).

## 5. Discussion

### 5.1. Depletion of Magnetic Minerals in Fault Rocks and Fluid Infiltration

Generally, cataclasite is formed at upper crustal levels (likely 10–15 km deep), whereas the fault breccia and gouge are formed at distinctly shallower depths of <5 km (cf. fault model of *Sibson* [1977]). Therefore, retrieval of both (proto-)cataclasites and fault breccia/gouge in the shallow drilling holes implies that fault zone has been exhumed from the upper crustal levels, and many earthquakes have occurred along the fault zone during its long-term exhumation history [*Ran et al.*, 2010]. It is also evidenced by a thermochronology study on the Pengguan complex [*Wang et al.*, 2012], which has revealed that the still on-going exhumation of eastern Tibet began at 30–25 Ma, and the rocks seen at the surface today originally resided at or above ~250°C, corresponding to a maximum depth of ~10–12 km. Studies of these fault rocks would thus shed light on the conditions in the fault zone during its evolution and exhumation history.

In a fault zone at shallow crustal levels, fault rocks are generally formed by brittle processes with moderate to high strain, which lead to fragmentation of the protolith, followed by granular flow and/or rolling of fragments, which induces further fragmentation [*Sibson*, 1977; *Hattori and Yamamoto*, 1999]. This process emerges from our microscopic observations of the fault rocks (Figure 4). It is argued that this process would also lead to widespread fragmentation of original magnetic grains (if present) into (much) finer size [*Hirono et al.*, 2006; *Mishima et al.*, 2009]. An elevated magnetic susceptibility would thus be expected in cataclastic rocks, once the grain size of crushed ferrimagnetic grains is finer than the SP/stable SD threshold [*Heider et al.*, 1996]. Otherwise, magnetic susceptibility of fault rocks should be more or less comparable with that of their protolith, if there has no other alteration occurred. In our study, SP-dominated and PSD magnetite in trace amounts are, respectively, identified in (proto-)cataclasite, and FWAG and granitic breccia (Figures 6 and 8), supporting the fragmentation of the preexisting MD magnetite in the granitic host rock by the cataclastic processes. This finding is also supported by the so-called King plot [*King et al.*, 1982], a bivariate plot of ARM susceptibility ( $\chi_{\text{ARM}}$ ) versus  $\chi_{\text{if}}$  (Figure 11). The  $\chi_{\text{ARM}}/\chi_{\text{if}}$  ratios increase significantly from the host rock, via FWAG to (proto-)cataclasite, suggesting a decrease in grain size of the magnetite [*King et al.*, 1982]. However, significant decreases in both magnetic susceptibilities ( $\chi_{\text{if}}$  and  $\chi_{\text{ferri}}$ ) and magnetization parameters ( $M_s$  and  $M_{rs}$ ) are observed as well from the host rock, via granitic breccia, FWAG, protocataclasite to cataclasite (Table 1), indicating that magnetite has been depleted during the cataclastic processes. Fault rocks show enriched volatile contents relative to the host rocks (Table 2) when approaching the fault core; this indicates that they are fluid-percolated zones [*Tanaka et al.*, 2001]. Significant mass-loss, which reflects the cumulative effects of mechanical wearing and fluid infiltration within a fault zone throughout its history [*Tanaka et al.*, 2001; *Chen et al.*, 2007], was revealed in the fault rocks here (Figure 10). These observations suggest that fault rocks in the drill cores have suffered pervasive fluid-rock interactions. It is supported by extensive fluid alteration structures (Figure 4), and increasing amounts of alteration products (e.g., chlorite and other clay minerals) in the fault rocks compared to the host rocks (Figure 9). Furthermore, it may well imply that fluid infiltration has widely occurred within the LMS fault zone during its entire long-term evolution and exhumation history.

**Table 2.** Average Bulk Geochemical Compositions of Fault Rocks and Host Rock (wt %)<sup>a</sup>

	Host Rock (n = 4)	Fault Breccia (n = 3)	FWAG (n = 5)	Protocataclasite (n = 4)	Cataclasite (n = 9)	YGG (n = 2)	BG (n = 9)	GGG (n = 5)
Na <sub>2</sub> O	5.62	2.28	4.17	5.80	5.42	1.71	0.30	1.83
MgO	1.05	3.31	1.64	1.25	1.19	8.64	3.71	7.19
Al <sub>2</sub> O <sub>3</sub>	15.15	14.98	15.43	15.37	15.39	15.69	12.53	14.74
SiO <sub>2</sub>	70.39	65.61	66.70	69.75	70.29	44.34	50.78	41.08
P <sub>2</sub> O <sub>5</sub>	0.09	0.12	0.13	0.10	0.10	0.58	0.25	0.55
K <sub>2</sub> O	2.31	2.79	2.34	2.17	1.86	2.14	2.33	0.49
CaO	1.66	1.68	2.68	1.27	1.64	1.98	10.24	5.53
TiO <sub>2</sub>	0.25	0.46	0.34	0.29	0.27	2.95	0.77	2.85
MnO	0.05	0.03	0.05	0.06	0.05	0.12	0.05	0.14
Fe <sub>2</sub> O <sub>3</sub>	0.74	0.82	0.49	0.66	0.44	1.56	1.31	3.23
FeO	1.36	2.40	2.12	1.71	1.68	12.09	2.84	12.18
H <sub>2</sub> O <sup>+</sup>	1.01	4.23	2.05	1.29	1.14	7.18	4.77	6.37
CO <sub>2</sub>	0.16	1.16	1.62	0.08	0.29	0.79	7.91	3.71
LOI	1.18	5.10	3.65	1.18	1.42	6.78	14.24	8.90

<sup>a</sup>Note: n, sample numbers used to calculate the average values; FWAG, fractured and weakly altered granite; YGG, yellow-green-gouge; BG, black-gouge; GGG, grey-green-gouge.

A simple conceptual model illustrating the most likely fluid-assisted cataclastic processes, which result in a significant decay in magnetization of fault rocks, is shown in Figure 12. With the fragmentation of the protolith (granite with magnetite as the dominant magnetic carrier), fluids infiltrate into the fault zone. Due to the granular flow and rolling of fragments, the grain size of the fragments is pervasively reduced, leading to a large specific surface. The fluid percolation causes intense fluid-rock reactions (e.g., breakdown of feldspars), as evidenced by the alteration and depletion of feldspars in fault rocks (Figures 4 and 9). With it, the magnetite in the intensely fractured granite would be also more prone to reaction with the fluids.

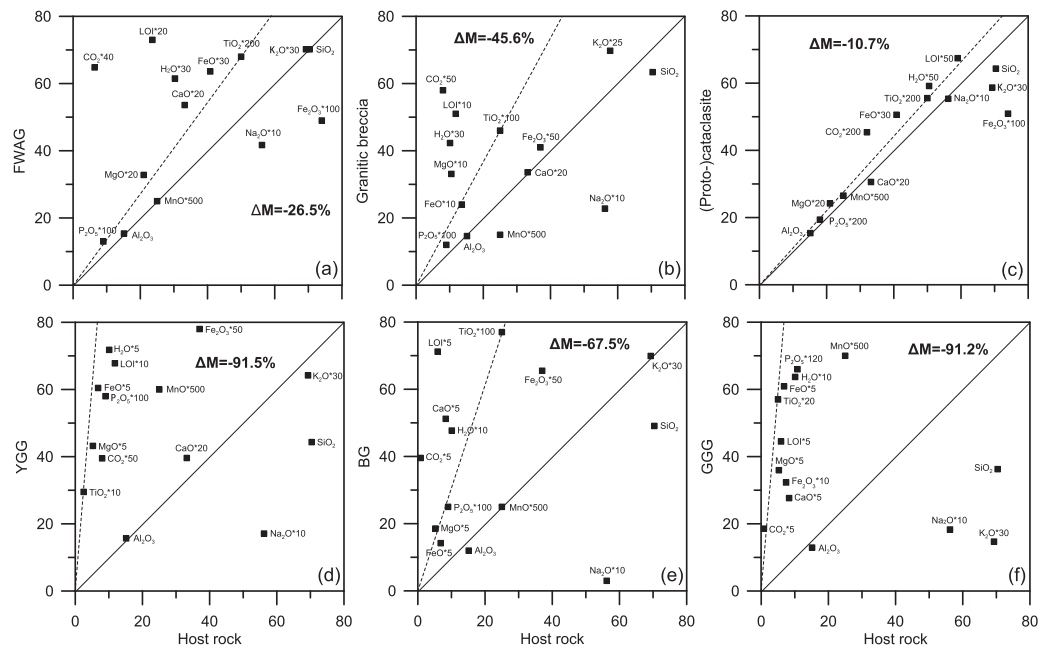


**Figure 10.** Grant-type plots for the host rock against the different fault rocks in the drill cores. Concentrations are noted for major elements in wt % and scaled to fit on the plot. For example, TiO<sub>2</sub> is multiplied by 100 in the altered samples and their nonaltered counterparts; otherwise the point would plot very close to the origin. The solid diagonal line in each plot is the 1:1 line of constant mass, along which compositions of altered fault rocks and unaltered host rock are identical. The dashed isocline line defined by the element considered immobile (here TiO<sub>2</sub>) is above the line of constant mass. This indicates that alteration is associated with mass loss; concentrations of immobile elements are increased due to mass loss. Compositions plotting above the dashed isocline indicate enrichment relative to the unaltered equivalent, whereas points below the isocline indicate depleted abundances; intermediate compositions (i.e., those along the isocline) indicate relative immobility. For convenience, group averages are plotted. See Table 2 for more details in the chemical composition variations.  $\Delta M$  (%) indicates the percentage mass loss relative to the host rock (see main text for calculation). FWAG, fractured and weakly altered granite; YGG, yellow-green-gouge; BG, black-gouge; GGG, grey-green-gouge.

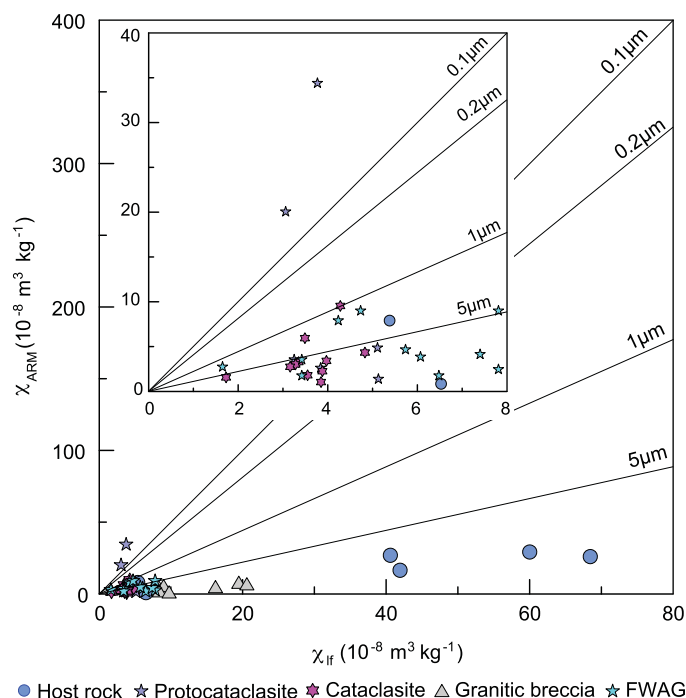


**Figure 11.** Bivariate-plot of ARM susceptibility ( $\chi_{ARM}$ ) versus low-field susceptibility ( $\chi_{lf}$ ) [King et al., 1982]. The inset shows a blow-up of the region near the origin (i.e., samples with  $\chi_{lf} < 8.0 \times 10^{-8} \text{ m}^3 \text{ kg}^{-1}$ ). The reference isopleth lines of grain size of magnetite particles are after King et al. [1982]. FWAG = fractured and weakly altered granite.

Destabilization of magnetite would release Fe that readily enters the fluid and is subsequently transported. The Fe-rich fluids are considered to be the sources for formation of Fe-bearing clay minerals (e.g., chlorite) as the alteration products. With the increasing cataclastic levels and more fluid percolation, more feldspars and magnetite would be depleted. Finally, only traces of magnetite survive, and more Fe-bearing alteration products occur in the newly formed fault rocks (e.g., cataclasite, fault breccia), which thus behave paramagnetically.

Anonymous high magnetic susceptibility values in seismic fault zones have been reported in several drilling projects carried out after major earthquakes, for example, the TCDP after the 1999 Chi-Chi earthquake [e.g., Hirono et al., 2006; Mishima et al., 2006], and the recent WFSD-1 project after the 2008 Wenchuan earthquake [e.g., Li et al., 2014; Pei et al., 2014a]. These drill-

ing projects were conducted immediately after the large earthquakes, thus one can identify these magnetic enhancements induced by seismic heating in the recent slip zone. However, as also revealed by the present study, fluid infiltration is widely present in a fault zone. Also during the long-term interseismic periods, fluids, either of meteoric or of deep origin (or a combination), infiltrate and percolate into the fault zone. Therefore, the latest coseismic imprinted magnetic records (i.e., the aforementioned high magnetic susceptibility) could be erased or overprinted. Thus, there would be a rare opportunity to gain crucial information by observing such transient changes related to a specific rupture only immediately after a large earthquake. The fault properties will be measurably changed 2 years after the earthquake [Brodsky et al., 2009]. Interseismic fluid infiltration would be one of the most important factors driving these changes.

### 5.2. Magnetic Indication of Rock-Fluid Interactions

Fault fluid-related dissolution-precipitation processes that are operative during co, post, and interseismic periods are commonly observed in fault zones [e.g., Gratier et al., 2011; Chen et al., 2013]. These processes favor clay mineral reactions and/or transformations in fault zones, such as chloritization and illitization [Isaacs et al., 2007; Kuo et al., 2009; Chen et al., 2013; Li et al., 2014]. Microscopic observations (Figure 4), magnetic measurements (e.g., thermomagnetic curves in Figure 6), and XRD analyses (Figure 9) identified iron sulfides (mostly pyrite) widely present in fault gouges. Meanwhile, total organic carbon (TOC) analysis revealed that the BG group has a maximum TOC content of 3.1%. Further XRD analysis of the samples after hydrofluoric and hydrochloric acid treatment indicates they are mostly amorphous or microcrystalline carbon. These observations suggest that the fault zone is anoxic, conditions that favor the formation of chlorite [Grosz et al., 2006; Bishop et al., 2008]. Chlorite, which is usually formed by hydrothermal alteration [e.g., Peters and Hofmann, 1984], occurs throughout the investigated fault rocks (Figures 4 and 9). Gypsum, which is another diagnostic mineral for hydrothermal processes [Tang et al., 2014], is also present occasionally within the fault core (Figure 9). Furthermore, considerable enrichment of volatile contents is present in the fault gouge zones (Table 2). All in all, this suggests a wide occurrence of hydrothermal activity in the active LMS fault zone.

Based on the relation between the basal spacing of chlorite and its crystallization temperature, formation temperature of chlorite in the studied fault rocks is inferred to be lower than  $\sim 100^\circ\text{C}$  (Duan, unpublished data,

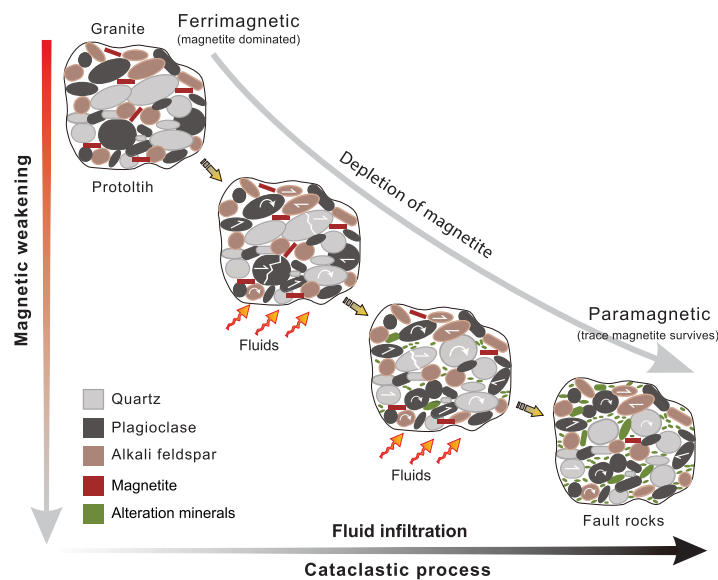


**Figure 12.** A simple conceptual model illustrating the fluid-assisted cataclastic process, which transforms the granite protolith (ferrimagnetic magnetite as the dominant magnetic carrier) to (paramagnetic) fault rocks (e.g., cataclasite, fault breccia, and gouge). On the fragmentation of the granite, the faulting-promoted fluids (assumed to be of deep origin and thus rather hot) infiltrate into and percolate within the fault zone. The grain size of the fragments is reduced by increasing cataclasis, leading to a high fluid-rock ratio. As such, magnetite in the fractured granite is more susceptible to reaction with and readily destabilized by the fluids. The released Fe enters fluids and is then precipitated in the newly formed alteration minerals (chlorite and other clay minerals). With increasing cataclasis and more fluid infiltration, more magnetite will be depleted. Finally, only traces of magnetite survive, and the fault rock is thus essentially paramagnetic. Schematized cataclasite processes and granite protolith are modified from Rowe and Griffith [2015].

2015). In this temperature range, the chlorite is prone to incorporate Fe, and Fe-rich chlorites are thus fairly common [Caritat et al., 1993; Haines, 2008]. In contrast, illitization of smectite releases considerable amounts of Fe [Drief et al., 2002; Osborn et al., 2014].  $\chi_{hf}$  of a sample largely depends on its Fe content [e.g., Nagata, 1961], and can thus be used as proxy of Fe content [e.g., Rochette et al., 1992; Ferré et al., 2012]. In the drill cores, both  $\chi_{lf}$  and  $\chi_{hf}$  of fault rocks are closely correlated with the clay mineral content (Table 3, Figure 13a and 13b), especially chlorite (Figures 13c and 13d). For example, the coefficient of determination ( $R^2$ ) between  $\chi_{hf}$  and clay minerals is 0.62, and that between  $\chi_{hf}$  and chlorite is 0.61 (Table 3).  $\chi_{lf}$  and  $\chi_{hf}$  are negatively correlated with illite (Figures 13e and 13f). These observations imply that repartitioning of Fe during the clay mineral reactions in fault zones is recorded by  $\chi_{hf}$ .

Meanwhile, the HFS elements (e.g.,  $TiO_2$ ,  $MnO$ ,  $MgO$ , and  $P_2O_5$ ) have been proposed to be less mobile or immobile even under intense fluid-rock interaction, and their concentration in fault zones reflect the losses of mobile elements by mechanical wear and dissolution, which result in mass (or volume) loss [Evans and Chester, 1995; Goddard and Evans, 1995; Tanaka et al., 2001; Chen et al., 2007]. Here both  $\chi_{lf}$  and  $\chi_{hf}$  are correlated strongly with those HFS elements, as well as  $H_2O^+$  (Table 4). For example,  $R^2$  between  $\chi_{lf}$  and  $TiO_2$  is 0.74, that between  $\chi_{lf}$  and  $P_2O_5$  is 0.70, while it is 0.53 between  $\chi_{lf}$  and  $H_2O^+$ , respectively (Figures 14a–14d).

In this study, the calculated mass loss of fault rocks is distinctly higher than that in other granite hosted [e.g., Tanaka et al., 2001], sedimentary rock-hosted [e.g., Chen et al., 2007], or gneiss-hosted [e.g., Evans and Chester, 1995] fault zones. For example, the mass loss is ~13.0% for fault breccia in the Nojima

**Table 3.** Coefficients of Determination ( $R^2$ ) of Linear Fit Between Magnetic Parameters, Content of Bulk and Clay Minerals in Fault Rocks ( $n = 29$ )

	Quartz	Feldspar	Calcite	Clay Mineral	Smectite	Illite	Chlorite
$\chi_{lf}$	0.23 <sup>a</sup>	0.63 <sup>a</sup>	0.10	0.68 <sup>a</sup>	0.36 <sup>b</sup>	0.01	0.69 <sup>a</sup>
$\chi_{hf}$	0.24 <sup>a</sup>	0.58 <sup>a</sup>	0.06	0.62 <sup>a</sup>	0.24 <sup>b</sup>	0.00	0.61 <sup>a</sup>
$\chi_{ferri}$	0.03	0.22	0.16 <sup>b</sup>	0.25 <sup>a</sup>	0.40 <sup>a</sup>	0.01	0.35 <sup>a</sup>
$\chi_{fd}^0$	0.01	0.64 <sup>a</sup>	0.03	0.27 <sup>a</sup>	0.07	0.05	0.17 <sup>b</sup>
ARM	0.04	0.24	0.06	0.13	0.28 <sup>b</sup>	0.12	0.10
$M_s$	0.00	0.08	0.12	0.06	0.18	0.02	0.06
$M_{fs}$	0.01	0.00	0.08	0.00	0.04	0.03	0.01
$B_c$	0.00	0.36 <sup>b</sup>	0.01	0.20 <sup>b</sup>	0.08	0.11	0.14 <sup>b</sup>
$B_{cr}$	0.01	0.36 <sup>b</sup>	0.23 <sup>a</sup>	0.18 <sup>b</sup>	0.29 <sup>b</sup>	0.08	0.07

<sup>a</sup>Correlation is significant at the 0.01 level.

<sup>b</sup>Correlation is significant at the 0.05 level.

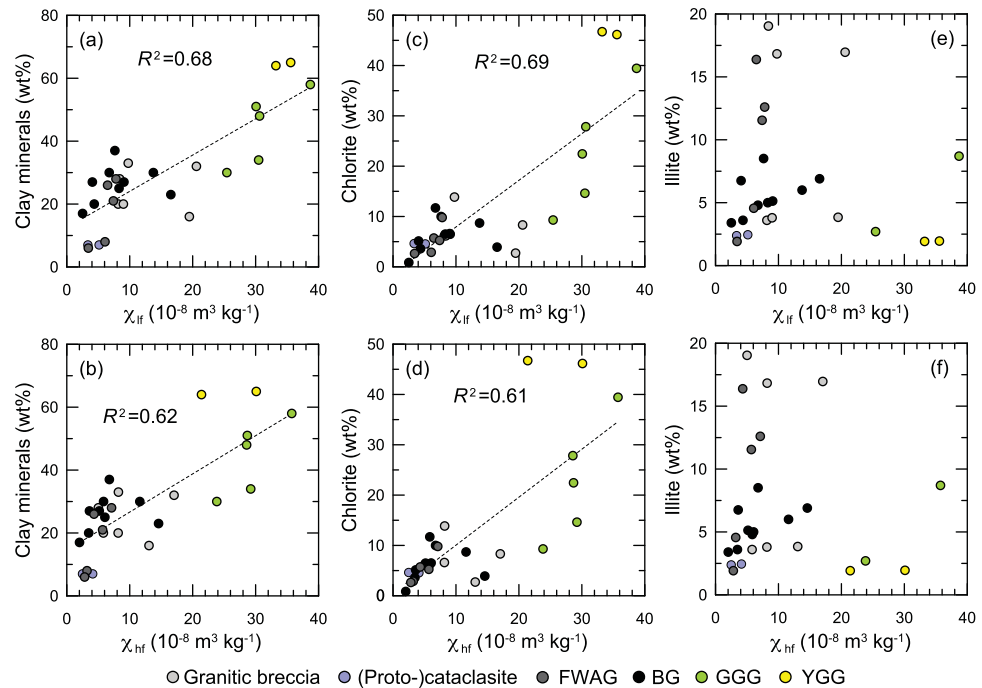


**Figure 13.** Relationships between both  $\chi_{lf}$  and  $\chi_{hf}$  with content of clay minerals, chlorite, and illite. Here weight percentages of chlorite and illite are normalized to bulk sample as  $\chi_{lf}$  and  $\chi_{hf}$  refer to the bulk samples. The reader is referred to Table 3 for details on the coefficients of determination ( $R^2$ ) between magnetic parameters, and bulk and clay minerals. FWAG, fractured and weakly altered granite; YGG, yellow-green-gouge; BG, black-gouge; GGG, grey-green-gouge.

fault (southwest Japan) which was activated during the 1995 Kobe earthquake [Tanaka et al., 2001]. It is ~42% for the gouge zone in the Chelungpu fault zone that accommodated the 1999 Chi-Chi earthquake [Chen et al., 2007]. However, it is comparable with those in the Pingxi (~90.6% for the

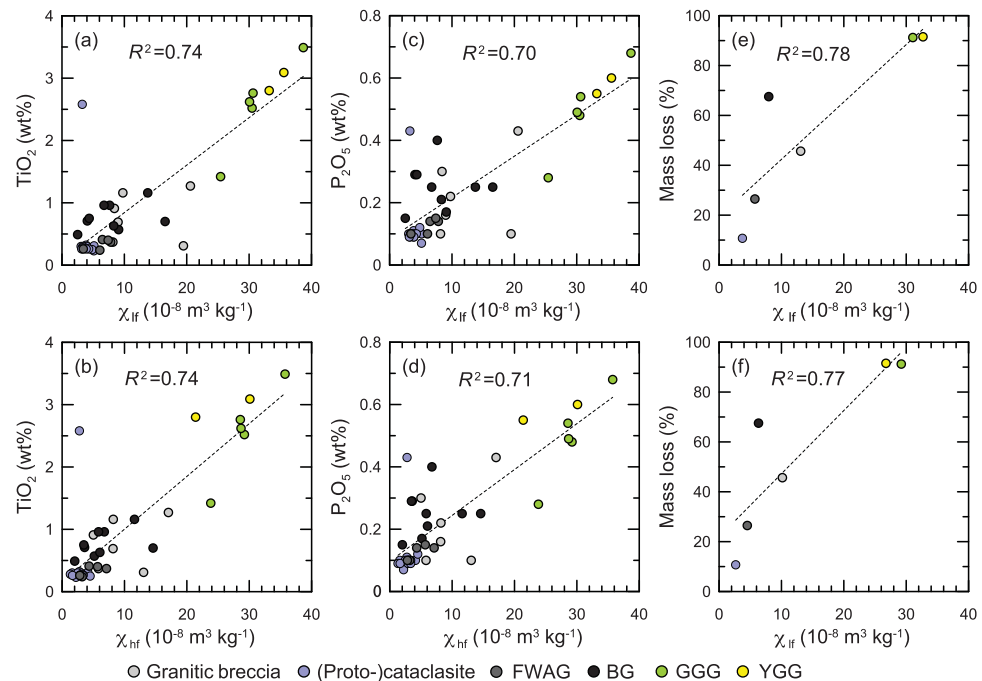


**Figure 14.** Relationships between both  $\chi_{lf}$  and  $\chi_{hf}$  with representative HFS elements, and mass losses obtained from isocon analysis (see Figure 10 for detailed values). The reader is referred to Table 4 for details on the coefficients of determination ( $R^2$ ) between magnetic parameters and chemical compositions. FWAG, fractured and weakly altered granite; YGG, yellow-green-gouge; BG, black-gouge; GGG, grey-green-gouge.

**Table 4.** Coefficients of Determination ( $R^2$ ) of Linear Fit Between Magnetic Parameters, Content of Major and Minor Oxides of Fault Rocks ( $n = 41$ )

	Na <sub>2</sub> O	MgO	Al <sub>2</sub> O <sub>3</sub>	SiO <sub>2</sub>	P <sub>2</sub> O <sub>5</sub>	K <sub>2</sub> O	CaO	TiO <sub>2</sub>	MnO	Fe <sub>2</sub> O <sub>3</sub>	FeO	H <sub>2</sub> O <sup>+</sup>	CO <sub>2</sub>	LOI
$\chi_{lf}$	0.18 <sup>a</sup>	0.58 <sup>a</sup>	0.00	0.40 <sup>a</sup>	0.70 <sup>a</sup>	0.22 <sup>a</sup>	0.01	0.74 <sup>a</sup>	0.29 <sup>a</sup>	0.35 <sup>a</sup>	0.73 <sup>a</sup>	0.53 <sup>a</sup>	0.01	0.08
$\chi_{hf}$	0.18 <sup>a</sup>	0.57 <sup>a</sup>	0.01	0.44 <sup>a</sup>	0.71 <sup>a</sup>	0.30 <sup>a</sup>	0.03	0.74 <sup>a</sup>	0.34 <sup>a</sup>	0.42 <sup>a</sup>	0.74 <sup>a</sup>	0.50 <sup>a</sup>	0.03	0.10 <sup>b</sup>
$\chi_{ferri}$	0.05	0.18 <sup>a</sup>	0.02	0.03	0.15 <sup>b</sup>	0.02	0.03	0.15 <sup>b</sup>	0.01	0.00	0.15 <sup>b</sup>	0.20 <sup>a</sup>	0.02	0.00
$\chi_{fd}\%$	0.31 <sup>a</sup>	0.22 <sup>a</sup>	0.02	0.20 <sup>a</sup>	0.28 <sup>a</sup>	0.00	0.04	0.20 <sup>a</sup>	0.02	0.07	0.19 <sup>a</sup>	0.35 <sup>a</sup>	0.05	0.14 <sup>b</sup>
ARM	0.07	0.13 <sup>b</sup>	0.10 <sup>b</sup>	0.18 <sup>a</sup>	0.10	0.08	0.12 <sup>b</sup>	0.10 <sup>b</sup>	0.04	0.01	0.08	0.12 <sup>b</sup>	0.11 <sup>b</sup>	0.15 <sup>b</sup>
$M_s$	0.11 <sup>b</sup>	0.16 <sup>a</sup>	0.00	0.04	0.08	0.00	0.00	0.08	0.00	0.01	0.09	0.26 <sup>a</sup>	0.00	0.02
$M_{rs}$	0.03	0.04	0.00	0.00	0.00	0.02	0.02	0.00	0.01	0.00	0.00	0.10 <sup>b</sup>	0.01	0.00
$B_c$	0.13 <sup>b</sup>	0.14 <sup>b</sup>	0.00	0.09	0.13 <sup>b</sup>	0.00	0.01	0.12 <sup>b</sup>	0.06	0.06	0.11 <sup>b</sup>	0.18 <sup>a</sup>	0.01	0.05
$B_{cr}$	0.28 <sup>a</sup>	0.19 <sup>a</sup>	0.03	0.18 <sup>a</sup>	0.16 <sup>a</sup>	0.01	0.04	0.13 <sup>b</sup>	0.04	0.13 <sup>b</sup>	0.12 <sup>b</sup>	0.30 <sup>a</sup>	0.05	0.14 <sup>b</sup>

<sup>a</sup>Correlation is significant at the 0.01 level.

<sup>b</sup>Correlation is significant at the 0.05 level.

gouge zone) and Zhaojiagou (~93.7% for the gouge zone) exposures along the YBF fault [Chen *et al.*, 2013]. This also reveals the accumulated effects of cataclasis and fluid infiltration during the long evolution history of the LMS fault zone. It is noteworthy that both  $\chi_{lf}$  and  $\chi_{hf}$  of fault rocks strongly correlate with the mass-losses (Figures 14e and 14f), with  $R^2$  of 0.78 and 0.77, respectively. These collective observations suggest that magnetic susceptibility can serve as an indication of Fe-partitioning as a consequence of clay mineral reactions associated with rock-fluid interactions in a seismically active fault zone, and magnetic studies into fault rocks can reveal rock-fluid interactions within a fault zone.

## 6. Conclusions

Detailed rock magnetic investigations combined with mineralogical and chemical analyses were conducted on fault rocks retrieved from the drill holes that penetrated the rupture zone of the 2008 Wenchuan earthquake on the Yingxiu-Beichuan fault (China). Results reveal distinctly varying magnetic properties, mineral assemblages and geochemical compositions in granitic host rock, granitic breccia and fault gouge, as well as (proto-)cataclasites. We conclude that these magnetic changes are closely associated with rock-fluid interactions during the faulting process. The main results from this study are summarized next.

1. Magnetic behavior of the granitic host rock is dominated by small MD magnetite. Trace amounts of PSD/SD+SP magnetite in all fault rocks confirm that their magnetic behavior is essentially controlled by the paramagnetic fraction.
2. Depletion of magnetite in fault rocks, and concomitant decreases in both low-field magnetic susceptibility and magnetization, is compatible with an increasing degree of alteration from the protolith, via (proto-)cataclasite to FWAG and granitic breccia. We document enriched volatile contents and amounts of alteration products (chlorite) relative to the host rocks toward the fault core, and have estimated significant mass-losses in the fault rocks. These observations imply that fluid infiltration has widely occurred within the LMS fault zone during its long-term evolution and exhumation history. This alteration is manifest in magnetite depletion within the fault rocks, a process that is recorded by an increase in paramagnetic behavior.
3. Close relationships (with coefficients of determination of ~0.60 and higher) are observed between both low and high-field magnetic susceptibility and the abundance of clay minerals, in particular chlorite which we infer to result from hydrothermal activity. Chlorite growth suggests that rock-fluid interactions control Fe partitioning and that the fate of magnetic minerals in fault rocks is linked to clay mineral reactions within fault zones.
4. Additional close relationships, with coefficient of determination of >0.70, between both low and high-field magnetic susceptibility and the HFS elements, H<sub>2</sub>O<sup>+</sup>, and mass-losses of fault rocks demonstrate that straight-forward, affordably measured magnetic properties can serve as proxy indicators of fluid-rock interactions within shallow fault zones.

### Acknowledgments

This study was supported by the State Key Laboratory of Earthquake Dynamics, Institute of Geology, China Earthquake Administration (grant LED2010A03), the Special Fund for Earthquake-Scientific Research in the Public Interest (grant 201508018), and the National Natural Science Foundation of China (grant 41204062). T. Yang acknowledges the China Scholarship Council (CSC) for a visiting scholarship to Utrecht University (The Netherlands). We would like to thank Charles Aubourg, Peter C. Lippert, and the Associate Editor Joshua Feinberg for their comments which helped to improve the manuscript. All data for this study are available from the corresponding author via email: yangtao@cea-igp.ac.cn, or t.yang@uu.nl.

### References

- Bishop, J. L., M. D. Lane, M. D. Dyar, and A. J. Brown (2008), Reflectance and emission spectroscopy study of four groups of phyllosilicates: Smectites, kaolinite-serpentines, chlorites and micas, *Clay Miner.*, *43*(1), 35–54.
- Brodsky, E., K.-F. Ma, J. Mori, D. M. Saffer, and the participants of the ICDP/SCEC International Workshop (2009), Rapid response fault drilling: Past, present and future, *Sci. Drill.*, *8*, 66–74.
- Caritat, P. de, I. Hutcheon, and J. L. Walshe (1993), Chlorite geothermometry: A review, *Clays Clay Miner.*, *41*(2), 219–239.
- Chen, J.-Y., X.-S. Yang, S.-L. Ma, and C. J. Spiers (2013), Mass removal and clay mineral dehydration/rehydration in carbonate-rich surface exposures of the 2008 Wenchuan Earthquake Fault: Geochemical evidence and implication for fault zone evolution and coseismic slip, *J. Geophys. Res. Solid Earth*, *118*, 474–496, doi:10.1002/jgrb.50089.
- Chen, W. D., H. Tanaka, H. Huang, C. Lu, C. Lee, and C. Wang (2007), Fluid infiltration associated with seismic faulting: Examining chemical and mineralogical compositions of fault rocks from the active Chelungpu fault, *Tectonophysics*, *443*(3–4), 243–254.
- Chou, Y.-M., S.-R. Song, C. Aubourg, Y.-F. Song, A.-M. Boullier, T.-Q. Lee, M. Evans, E.-C. Yeh, and Y.-M. Chen (2012a), Pyrite alteration and neofomed magnetic minerals in the fault zone of the Chi-Chi earthquake (Mw 7.6, 1999): Evidence for frictional heating and co-seismic fluids, *Geochim. Geophys. Geosyst.*, *13*, Q08002, doi:10.1029/2012GC004120.
- Chou, Y.-M., S.-R. Song, C. Aubourg, T.-Q. Lee, A.-M. Boullier, Y.-F. Song, E.-C. Yeh, L.-W. Isaacs, and C.-Y. Wang (2012b), An earthquake slip zone is a magnetic recorder, *Geology*, *40*(6), 551–554.
- Day, R., M. Fuller, and V. A. Schmidt (1977), Hysteresis properties of titanomagnetites: Grain-size and compositional dependence, *Phys. Earth Planet. Inter.*, *13*(4), 260–267.
- Dearing, J. A., K. L. Hay, S. M. J. Baban, A. S. Huddleston, E. M. H. Wellington, and P. J. Loveland (1996), Magnetic susceptibility of soil: An evaluation of conflicting theories using a national data set, *Geophys. J. Int.*, *127*(3), 728–734.
- Drief, A., F. Martinez-Ruiz, F. Nieto, and N. Velilla Sanchez (2002), Transmission electron microscopy evidence for experimental illitization of smectite in K-enriched seawater solution at 50°C and basic pH, *Clays Clay Miner.*, *50*(6), 746–756.
- Duan, Q.-B., X.-S. Yang, S.-L. Ma, J.-Y. Chen, and J.-Y. Chen (2016), Fluid–rock interactions in seismic faults: Implications from the structures and mineralogical and geochemical compositions of drilling cores from the rupture of the 2008 Wenchuan earthquake, China, *Tectonophysics*, *666*, 260–280.
- Dunlop, D. J. (2002), Theory and application of the Day plot ( $M_r/M_s$  versus  $H_{cr}/H_c$ ): 1. Theoretical curves and tests using titanomagnetite data, *J. Geophys. Res.*, *107*(B3), 2056, doi:10.1029/2001JB000486.
- Dunlop, D. J., and Ö. Özdemir (1997), *Rock Magnetism: Fundamentals and Frontiers*, Cambridge Univ. Press, Cambridge.
- Enomoto, Y., and Z. Zheng (1998), Possible evidences of earthquake lightning accompanying the 1995 Kobe earthquake inferred from the Nojima fault gouge, *Geophys. Res. Lett.*, *25*(14), 2721–2724.
- Evans, J. P., and F. M. Chester (1995), Fluid-rock interaction in faults of the San Andreas system: Inferences from San Gabriel Fault rock geochemistry and microstructures, *J. Geophys. Res.*, *100*(B7), 13,007–13,020.
- Ferré, E. C., M. S. Zechmeister, J. W. Geissman, N. MathanaSekaran, and K. Kocak (2005), The origin of high magnetic remanence in fault pseudotachylites: Theoretical considerations and implication for coseismic electrical currents, *Tectonophysics*, *402*(1–4), 125–139.
- Ferré, E. C., J. W. Geissman, and M. S. Zechmeister (2012), Magnetic properties of fault pseudotachylites in granites, *J. Geophys. Res.*, *117*, B01106, doi:10.1029/2011JB008762.
- Fukuchi, T. (2003), Strong ferrimagnetic resonance signal and magnetic susceptibility of the Nojima pseudotachylite in Japan and their implication for coseismic electromagnetic changes, *J. Geophys. Res.*, *108*(B6), 2312, doi:10.1029/2002JB002007.
- Goddard, J. V., and J. P. Evans (1995), Chemical changes and fluid-rock interaction in faults of crystalline thrust sheets, northwestern Wyoming, U.S.A., *J. Struct. Geol.*, *17*(4), 533–547.
- Goldstein, A. G., and L. L. Brown (1988), Magnetic susceptibility anisotropy of mylonites from the Brevard Zone, North Carolina, U.S.A., *Phys. Earth Planet. Inter.*, *51*(4), 290–300.
- Grant, J. A. (1986), The isocon diagram: A simple solution to Gresens' equation for metasomatic alteration, *Econ. Geol.*, *81*(8), 1976–1982.
- Gratier, J.-P., J. Richard, F. Renard, S. Mitterpergher, M.-L. Doan, G. Di Toro, J. Hadizadeh, and A.-M. Boullier (2011), Aseismic sliding of active faults by pressure solution creep: Evidence from the San Andreas Fault Observatory at Depth, *Geology*, *39*(12), 1131–1134.
- Grosz, S., A. Matthews, S. Ilani, A. Ayalon, and Z. Garfunkel (2006), Iron mineralization and dolomitization in the Paran Fault zone, Israel: Implications for low-temperature basinal fluid processes near the Dead Sea Transform, *Geofluids*, *6*(2), 137–153.
- Guichet, X., L. Jouniaux, and N. Catel (2006), Modification of streaming potential by precipitation of calcite in a sand-water system: Laboratory measurements in the pH range from 4 to 12, *Geophys. J. Int.*, *166*(1), 445–460.
- Haines, S. (2008), Transformations in clay-rich fault rocks: Constraining fault zone processes and the kinematic evolution of regions, PhD thesis, 295 pp., Univ. Michigan, Ann Arbor.
- Hashimoto, Y., and U. Kaji (2012), Rock-fluid interaction along seismogenic faults inferred from clay minerals in Okitsu melange, the Cretaceous Shimanto Belt, SW Japan, in *Earthquake Research and Analysis: Seismology, Seismotectonic and Earthquake Geology*, edited by S. D'Amico, pp. 253–270, InTech, Rijeka, Croatia.
- Hattori, I., and H. Yamamoto (1999), Rock fragmentation and particle size in crushed zones by faulting, *J. Geol.*, *107*(2), 209–222.
- Heider, F., A. Zitelsberger, and K. Fabian (1996), Magnetic susceptibility and remanent coercive force in grown magnetite crystals from 0.1  $\mu\text{m}$  to 6 mm, *Phys. Earth Planet. Inter.*, *93*(3–4), 239–256.
- Hickman, S., R. Sibson, and R. Bruhn (1995), Introduction to special section: Mechanical involvement of fluids in faulting, *J. Geophys. Res.*, *100*(B7), 12,831–12,840.
- Hirono, T., et al. (2006), High magnetic susceptibility of fault gouge within Taiwan Chelungpu fault: Nondestructive continuous measurements of physical and chemical properties in fault rocks recovered from Hole B, TCDP, *Geophys. Res. Lett.*, *33*, L15303, doi:10.1029/2006GL026133.
- Isaacs, A. J., J. P. Evans, S.-R. Song, and P. T. Kolesar (2007), Structural, mineralogical, and geochemical characterization of the Chelungpu thrust fault, Taiwan, *Terr. Atmos. Ocean. Sci.*, *18*(2), 183–221.
- Ishikawa, T., et al. (2008), Coseismic fluid-rock interactions at high temperatures in the Chelungpu fault, *Nat. Geosci.*, *1*, 679–683.
- Johnson, K. M., A. E. King, and J. M. Sieburth (1985), Coulometric TCO<sub>2</sub> analyses for marine studies; an introduction, *Mar. Chem.*, *16*(1), 61–82.
- Just, J., and A. Kontny (2012), Thermally induced alterations of minerals during measurements of the temperature dependence of magnetic susceptibility: A case study from the hydrothermally altered Soutz-sous-Forêts granite, France, *Int. J. Earth Sci.*, *101*(3), 819–839.
- Kerrich, R., and D. C. Kamineni (1988), Characteristics and chronology of fracture—fluid infiltration in the Archean, Eye Dashwa Lakes pluton, Superior Province: Evidence from H, C, O-isotopes and fluid inclusions, *Contrib. Mineral. Petrol.*, *99*(4), 430–445.

- King, J. W., S. K. Banerjee, J. Marvin, and Ö Özdemir (1982), A comparison of different magnetic methods of determining the relative grain size of magnetite in natural materials: Some results from lake sediments, *Earth Planet. Sci. Lett.*, *59*(2), 404–419.
- Kuo, L.-W., S.-R. Song, E.-C. Yeh, and H.-F. Chen (2009), Clay mineral anomalies in the fault zone of Chelungpu Fault, Taiwan, and its implication, *Geophys. Res. Lett.*, *36*, L18306, doi:10.1029/2009GL039269.
- Li, H.-B., et al. (2014), Structural and physical property characterization in the Wenchuan earthquake Fault Scientific Drilling project -hole 1 (WFSD-1), *Tectonophysics*, *619–620*, 86–100.
- Lin, X., F. Ying, and N. Zheng (1992), *Techniques of X-Ray Diffraction Analysis and its Geological Application [In Chinese with English abstract]*, pp. 119–131, Pet. Ind. Press, Beijing.
- Liu, D.-L., H.-B. Li, T.-Q. Lee, Y.-M. Chou, S.-R. Song, Z.-M. Sun, M.-L. Chevalier, and J.-L. Si (2014), Primary rock magnetism for the Wenchuan earthquake fault zone at Jiulong outcrop, Sichuan Province, China, *Tectonophysics*, *619–620*, 58–69.
- Liu-Zeng, J., et al. (2009), Co-seismic ruptures of the 12 May 2008, Ms 8.0 Wenchuan earthquake, Sichuan: East-west crustal shortening on oblique, parallel thrusts along the eastern edge of Tibet, *Earth Planet. Sci. Lett.*, *286*(3–4), 355–370.
- Mishima, T., T. Hirono, W. Soh, and S.-R. Song (2006), Thermal history estimation of the Taiwan Chelungpu fault using rock-magnetic methods, *Geophys. Res. Lett.*, *33*, L23311, doi:10.1029/2006GL028088.
- Mishima, T., T. Hirono, N. Nakamura, W. Tanikawa, W. Soh, and S.-R. Song (2009), Changes to magnetic minerals caused by frictional heating during the 1999 Taiwan Chi-Chi earthquake, *Earth Planets Space*, *61*(6), 797–801.
- Mullender, T. A. T., A. J. van Velzen, and M. J. Dekkers (1993), Continuous drift correction and separate identification of ferrimagnetic and paramagnetic contribution in thermomagnetic runs, *Geophys. J. Int.*, *114*(3), 663–672.
- Nagata, T. (1961), *Rock Magnetism*, 2nd ed., 354 pp., Maruzen, Tokyo.
- Niwa, M., Y. Mizuochi, and A. Tanase (2015), Changes in chemical composition caused by water–rock interactions across a strike-slip fault zone: Case study of the Atera Fault, Central Japan, *Geofluids*, *15*(3), 387–409.
- Osborn, S. G., L. T. Duffield, W. C. Elliott, J. M. Wampler, R. D. Elmore, and M. H. Engel (2014), The timing of diagenesis and thermal maturation of the Cretaceous Marias River Shale, Disturbed Belt, Montana, *Clays Clay Miner.*, *62*(2), 112–125.
- Pechersky, D. M., and Y. S. Genshaft (2001), Petromagnetism of the continental lithosphere and the origin of regional magnetic anomalies: A review, *Russ. J. Earth Sci.*, *3*(2), 97–124.
- Pei, J.-L., H.-B. Li, H. Wang, J.-L. Si, Z.-M. Sun, and Z.-Z. Zhou (2014a), Magnetic properties of the Wenchuan Earthquake Fault Scientific Drilling Project Hole-1 (WFSD-1), Sichuan Province, China, *Earth Planets Space*, *66*, 23, doi:10.1186/1880-5981-66-23.
- Pei, J.-L., Z.-Z. Zhou, S.-G. Dong, and L. Tang (2014b), Magnetic evidence revealing frictional heating from fault rocks in granites, *Tectonophysics*, *637*, 207–217.
- Peters, T., and B. Hofmann (1984), Hydrothermal clay mineral formation in a biotite–granite in northern Switzerland, *Clay Miner.*, *19*(4), 579–590.
- Ran, Y.-K., L.-C. Chen, J. Chen, H. Wang, G.-H. Chen, J.-H. Yin, X. Shi, C.-X. Li, and X.-W. Xu (2010), Paleoseismic evidence and repeat time of large earthquakes at three sites along the Longmenshan fault zone, *Tectonophysics*, *491*, 141–153.
- Rao, T. G., and P. K. Govil (1995), Merits of using barium as a heavy absorber in major element analysis of rock samples by X-ray fluorescence: New data on ASK4 and ASK-2 reference samples, *Analyst*, *120*, 1279–1282.
- Rochette, P., M. Jackson, and C. Aubourg (1992), Rock magnetism and the interpretation of anisotropy of magnetic susceptibility, *Rev. Geophys.*, *30*(3), 209–226.
- Rowe, C. D., and W. A. Griffith (2015), Do faults preserve a record of seismic slip: A second opinion, *J. Struct. Geol.*, *78*, 1–26.
- Si, J.-L., H.-B. Li, L.-W. Kuo, J.-L. Pei, S.-R. Song, and H. Wang (2014), Clay mineral anomalies in the Yingxiu-Beichuan fault zone from the WFSD-1 drilling core and its implication for the faulting mechanism during the 2008 Wenchuan earthquake (Mw 7.9), *Tectonophysics*, *619–620*, 171–178.
- Sibson, R. H. (1977), Fault rocks and fault mechanisms, *J. Geol. Soc. London*, *133*, 191–214.
- Tanaka, H., K. Fujimoto, T. Ohtani, and H. Ito (2001), Structural and chemical characterization of shear zones in the freshly activated Nojima Fault Awaji Island, southwest Japan, *J. Geophys. Res.*, *106*(B4), 8789–8810.
- Tang, M., A. Ehreiser, and Y.-L. Li (2014), Gypsum in modern Kamchatka volcanic hot springs and the Lower Cambrian black shale: Applied to the microbial-mediated precipitation of sulfates on Mars, *Am. Mineral.*, *99*(10), 2126–2137.
- Tanikawa, W., T. Mishima, T. Hirono, W. Soh, and S.-R. Song (2008), High magnetic susceptibility produced by thermal decomposition of core samples from the Chelungpu fault in Taiwan, *Earth Planet. Sci. Lett.*, *272*(1–2), 372–381.
- Wang, E., E. Kirby, K. P. Furlong, M. V. Soest, G. Xu, X. Shi, P. Kamp, and K. V. Hodges (2012), Two-phase growth of high topography in eastern Tibet during the Cenozoic, *Nat. Geosci.*, *5*(9), 640–645.
- Wang, H., H.-B. Li, C. Janssen, Z.-M. Sun, and J.-L. Si (2015), Multiple generations of pseudotachylite in the Wenchuan fault zone and their implications for coseismic weakening, *J. Struct. Geol.*, *74*, 159–171.
- Xu, Z.-Q., S.-C. Ji, H.-B. Li, L.-W. Hou, X.-F. Fu, and Z.-H. Cai (2008), Uplift of the Longmen Shan range and the Wenchuan earthquake, *Episodes*, *31*(3), 291–301.
- Xu, X.-W., X.-Z. Wen, G.-H. Yu, G.-H. Chen, Y. Klinger, J. Hubbard, and J. H. Shaw (2009), Coseismic reverse- and oblique-slip surface faulting generated by the 2008 Mw 7.9 Wenchuan earthquake, China, *Geology*, *37*(6), 515–518.
- Yamaguchi, A., S. F. Cox, G. Kimura, and S. Okamoto (2011), Dynamic changes in fluid redox state associated with episodic fault rupture along a megasplay fault in a subduction zone, *Earth Planet Sci. Lett.*, *302*(3–4), 369–377.
- Yan, Q. R., et al. (2004), Neoproterozoic Subduction and Rifting on the Northern Margin of the Yangtze Plate, China: Implications for Rodinia Reconstruction, *Int. Geol. Rev.*, *46*(9), 817–832.
- Yang, T., J.-Y. Chen, H.-Q. Wang, and H.-Q. Jin (2012a), Rock magnetic properties of fault rocks from the rupture of the 2008 Wenchuan Earthquake, China and their implications: Preliminary results from the Zhaojiagou outcrop, Beichuan County (Sichuan), *Tectonophysics*, *530–531*, 331–341.
- Yang, T., J.-Y. Chen, H.-Q. Wang, and H.-Q. Jin (2012b), Magnetic properties of fault rocks from the Yingxiu-Beichuan fault: Constraints on temperature rise within the shallow slip zone during the 2008 Wenchuan Earthquake and their implications, *J. Asian Earth Sci.*, *50*, 52–60.
- Yang, T., J.-Y. Chen, X.-S. Yang, H.-Q. Wang, and H.-Q. Jin (2013), Differences in magnetic properties of fragments and matrix of breccias from the rupture of the 2008 Wenchuan earthquake, China: Relationship to faulting, *Tectonophysics*, *601*, 112–124.
- Zoback, M. D., S. Hickman, and W. Ellsworth (2007), The role of fault zone drilling, in *Earthquake Seismology: Treatise on Geophysics*, vol.4, edited by H. Kanamori and G. Schubert, pp. 649–674, Elsevier, Amsterdam.